ACS NANO

www.acsnano.org

ARTICLE

# Biomass-Based Nanoengineered Cooling Geotextile for Permafrost Thawing Prevention

Wenhui Xu,[▽] Xiaojie Liu,[▽] Wei Yan,[▽] Yanpei Tian,[▽] Yiming Xu, Wenkai Zhu, Noor M. Mohammad, Zhenyuan Niu, Ya Liu, Pengfei Deng, Qilong Cheng, Fengyin Du, Jinlong He, Hengxue Xiang, Ying Li, Jeffrey P. Youngblood, Nathan T. Kurtz, Meifang Zhu, Qianlai Zhuang, and Tian Li*

Cite This: *ACS Nano* 2025, 19, 40774–40788

Read Online

ACCESS | Metrics & More | Article Recommendations | Supporting Information

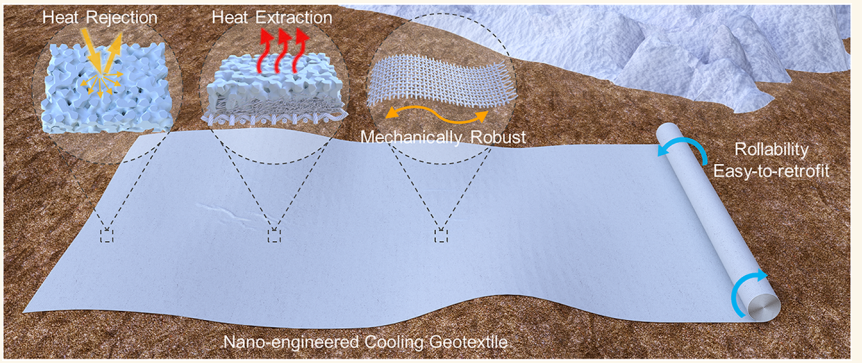


**ABSTRACT:** **Permafrost thawing is a critical climate tipping point, with catastrophic consequences. Existing stabilization methods rely on refrigerant-based systems, such as thermosyphons and active refrigeration, which are capital-intensive, energy-demanding, or increasingly ineffective in warming climates. Most infrastructure built on permafrost requires continuous heat removal from the foundation as the underlying permafrost becomes progressively unstable. To address these challenges, we demonstrate a fully biomass-derived cooling geotextile that can effectively mitigate permafrost thawing through scalable nanoprocessing via a roll-to-roll fabrication (1.3 m·min$^{-1}$). The cooling geotextile features a hierarchical three-layer design: a strong woven biomass scaffold, a permeable nonwoven fiber network, and an optimized porous coating layer with micro- and nano-structures. When anchored to bare ground, it extracts heat to the cold sky, enhances albedo from ∼30% to 96.3%, and establishes a thermal barrier between soil and air. Engineered for Arctic durability, it withstands strong winds, extreme cold, and freeze−thaw cycles, exceeding the American National Engineering Handbook requirements (tensile strength 1,682 kg; tear strength 191 kg; puncture strength 61 kg). Field tests in West Lafayette, IN (40°25′21″N, 86°55′12″W) reveal up to 25 °C soil cooling under 500 W·m$^{-2}$ irradiance. Its lightweight (0.8 kg·m$^{-2}$) and rollable attributes enable scalable and fast localized deployment. Simulations predict up to 12 °C surface cooling during Arctic summer (2020−2050), preventing up to 40,000 km$^2$ of permafrost from thawing. Completely derived from biomass, cooling geotextile ensures a low carbon footprint (0.7 kg·m$^{-2}$), positioning itself as a sustainable solution for reinforcing Arctic coastline, reconstructing thawing landscape, and restoring the environment.**

**KEYWORDS:** *permafrost thawing prevention, Arctic region, biomass materials, cooling geotextile, nanoengineering*

## INTRODUCTION

Permafrost, a layer of soil that remains at or below 0 °C for two or more consecutive years, covers approximately one-fifth of the northern hemisphere's exposed land[1] and stores more than 50% of global terrestrial carbon.[2,3] However, with cumulative impacts from global climate change, the Arctic is warming four times faster than the global average (Figure 1a), and the permafrost is rapidly thawing, threatening wildlife[4] and triggering carbon emission,[5,6] coastline erosion,[7] floods,[8]

Received: April 18, 2025
Revised: October 27, 2025
Accepted: October 28, 2025
Published: November 20, 2025

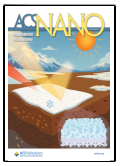

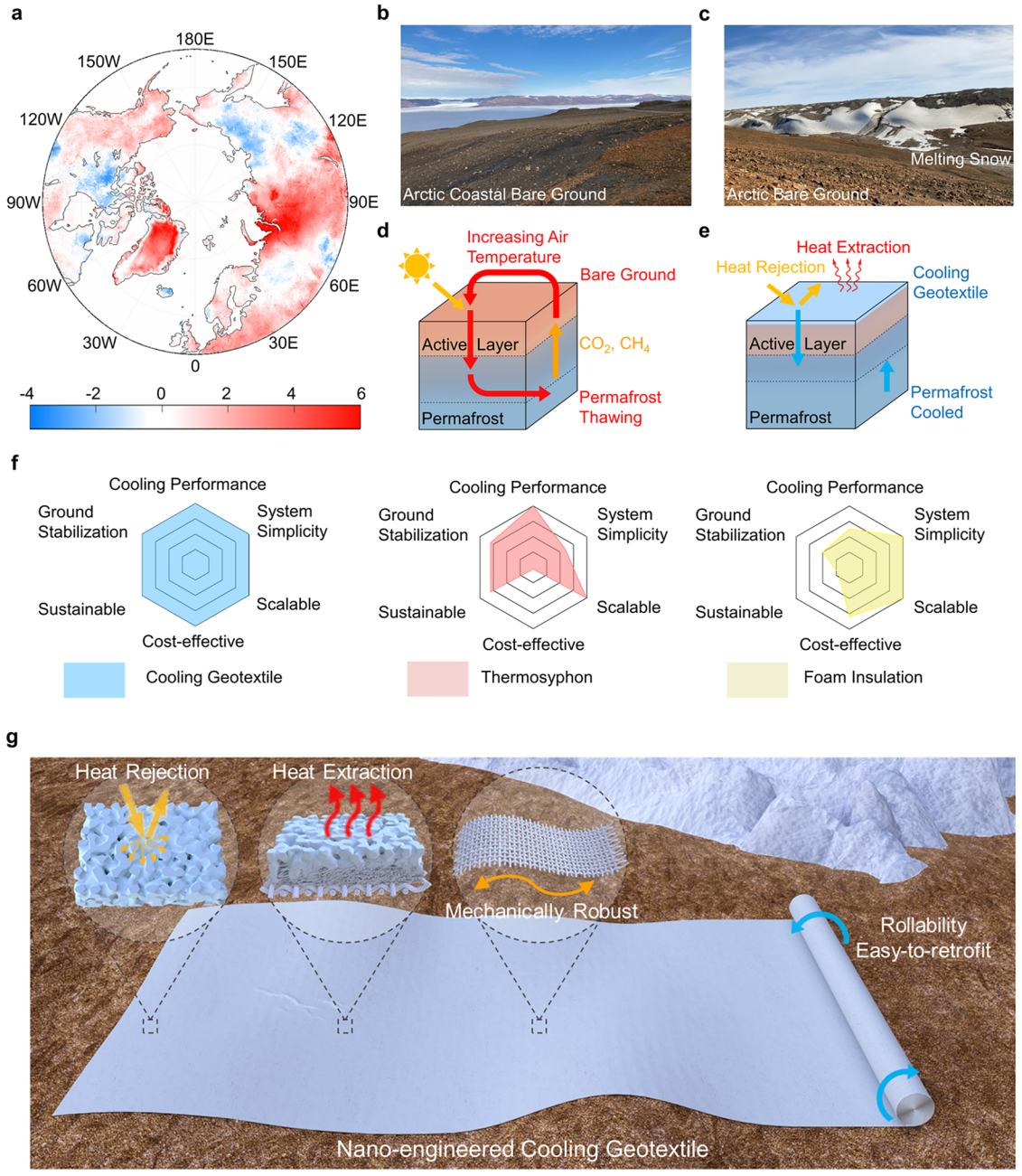


**Figure 1. Preventing permafrost from thawing by a cooling geotextile. (a) The pan-Arctic soil temperature rise from 2000 to 2016.[45] (b) The bare coastal soils and (c) exposed ground without snow cover in northern Greenland during the warming Arctic summer. (d) Schematics of permafrost thawing under direct solar radiation and the accelerated carbon release. (e) Illustration of cooling permafrost by simultaneous heat rejection, radiative cooling, and thermal insulation enabled by a deployed cooling geotextile. (f) Radar plots comparing the normalized performance of the cooling geotextile, thermosyphon, and foam insulation. (g) Schematics of a high-albedo, passive cooling, easy-to-retrofit, and rollable cooling geotextile covering the bare ground in the Arctic region.**

disease spread,[9,10] release of harmful chemicals[11] and heavy metals,[12] and destabilization of landscapes and buildings[13,14] (Figure 1b,1c). In addition, the mean annual erosion rate of permafrost coasts has more than doubled since the early 2000s due to anthropogenic warming,[15] which is expected to accelerate in response to further climate warming (Figures S1−S3). Failure to address permafrost protection will lead to catastrophic points of no return, as the weather pattern would easily fall into a vicious cycle (Figure 1d).[16−18] Therefore, preventing permafrost from thawing is vital for saving the Arctic and mitigating global warming.

Extensive investigations to alleviate these challenges rely on two main strategies: heat rejection and heat extraction.[19] Heat rejection method aims to reduce or even eliminate the heat transfer from the sun and air toward the permafrost via shading or insulating, such as the injection of sulfate aerosols into the stratosphere to increase Earth's albedo[20] and urea insulation foam with low thermal conductivity.[21] Heat extraction strategies, such as ventilation,[22] refrigeration,[23] and thermosyphon,[24] dissipate heat from the soil either actively or passively to cool the permafrost. Specifically, the widely used thermosyphon tubes utilize the evaporation and condensation


https://doi.org/10.1021/acsnano.5c06567
ACS Nano 2025, 19, 40774−40788

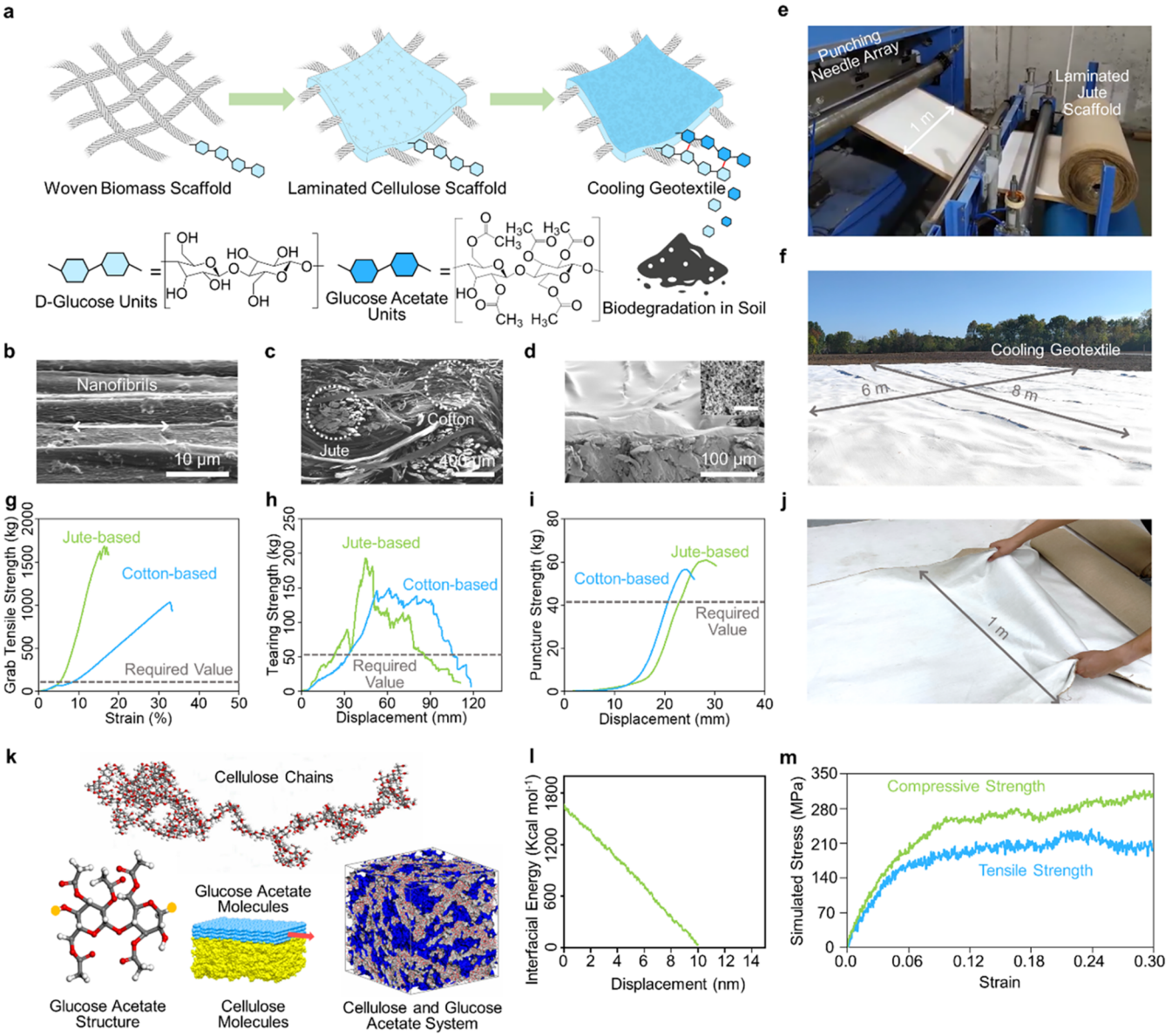


**Figure 2. Fabrication and characterization of cooling geotextile. (a) Schematics of the three-layer structure of the cooling geotextile using a woven biomass scaffold, nonwoven cotton fiber layer, and CA porous layer by solvent quenching, and its biodegradation in soil. (b–d) SEM images of (b) aligned nanofibrils on jute fibers, (c) the interface of the cotton laminated jute scaffold, and (d) micro- and nanoscale porous structure of CA coating on cooling geotextile. (e) Photo showing the large-scale fabrication process: the feeding and needle punching of woven jute scaffold and nonwoven cotton fiber layer, forming entangled laminated jute scaffold. (f) Photograph of a large-scale deployment of the cooling geotextile on the bare ground. (g–i) Mechanical strength of the NEH requirements, cotton- and jute-based cooling geotextiles: (g) grab tensile strength, (h) trapezoidal tear strength, and (i) photograph showing the flexibility of the cooling geotextile. (k) Atomistic models of cellulose chains, glucose acetate structures, CA-cotton cellulose system, and cellulose and glucose acetate system. (l) Steered molecular dynamics (SMD) simulation of the interfacial energy of hydrogen bonding between molecules of CA and cotton cellulose. The inserted figure shows the simulation model of the interfacial displacement between cotton cellulose and the CA layer ($10 \times 10 \times 5$ nm$^3$) during the pulling-out process. (m) Simulated tensile strength and compressive strength of the cellulose and CA chains.**

cycle of a pressurized liquid[25] to transfer heat (92–207 W·m$^{-2}$)[26] from the permafrost layer to the environment (Table S3), but their high installation cost and potential fluid leakage limit the large-scale applications in the fragile Arctic ecosystem.

Radiative cooling opens new opportunities for permafrost protection. Recently, radiative cooling materials or geotextiles have also been applied for glacier protection;[27−30] however, applying them to permafrost presents additional challenges, such as soil erosion and landscape collapse, highlighting the need for robust and resilient geotextile materials. Moreover, strong winds (~25 m·s$^{-1}$) and yearly freeze–thaw cycles (−37 to 24 °C at Utqiaġvik, Alaska, in 2023) require mechanically robust and thermally stable materials. Hence, it is imperative to develop easy-to-retrofit, reliable, and sustainable approaches to mitigating permafrost thawing in a cost-effective and eco-friendly deployment manner.

In this work, we demonstrate a scalable and biodegradable cooling geotextile to protect the thawing permafrost through three key mechanisms: increasing ground albedo, facilitating passive cooling, and enhancing thermal insulation. The cooling


https://doi.org/10.1021/acsnano.5c06567
ACS Nano 2025, 19, 40774−40788

geotextile rejects 96.3% solar irradiance by backscattering the intense sunlight through its micro- and nanoporous structures (Figure 1e), which surpasses the performance of most natural materials like fresh snow (typically 80−90%).[31−35] And the cooling geotextile spontaneously and passively cools itself by emitting thermal radiation with a thermal emittance of 93% to outer space through the atmospheric window (8−13 $\mu$m). Additionally, the low thermal conductivity of the cooling geotextile (0.028 $W{\cdot}m^{-1}{\cdot}K^{-1}$) renders it an effective thermal barrier, protecting permafrost from temperature rising in the Arctic summer.

Beyond radiative cooling, the proposed cooling geotextile also features sustainability and cost-effectiveness. All components are derived from biomass, making them biodegradable with minimized ecological impact. Notably, it offers a cost advantage compared with thermosyphon (>150 $\${\cdot}m^{-2}$) and urea foam (∼10 $\${\cdot}m^{-2}$) (Table S3), with lower fabrication costs of ∼$3.38 and $4.57 $m^{-2}$ for the cotton- and jute-based cooling geotextiles, respectively. A normalized comparative analysis (Figure 1f and Table S3) further indicates the sustainability and low cost of the cooling geotextile compared with conventional urea foam insulation.

To withstand harsh Arctic weather with strong winds and periodic freeze−thaw cycles, mechanical robustness is necessary for large-scale geotextile applications. From macroscopic woven patterns of fabrics down to nanofibrils and nanopores, the cooling geotextile is hierarchically engineered, with a higher mechanical strength (∼165 MPa) compared to biodegradable synthetic geotextiles such as polylactic acid (47−70 MPa), polyhydroxyalkanoates (18−35 MPa), and thermoplastic starch (10−56 MPa) (Table S4).[36−38] Therefore, the cooling geotextile can be firmly anchored locally to mitigate permafrost degradation and land subsidence (Figure 1g)[39] caused by disturbances from infrastructure as well as localized natural events (e.g., thermokarst formation,[40,41] thermal erosion,[6,42] and detachment slides[43,44]).

## RESULTS AND DISCUSSION

**Cooling Geotextile Preparation and Structure Characteristics.** Cellulose, the most abundant natural polymer,[46] constitutes approximately 90% of cotton fibers.[47] Characterized by a theoretical modulus from 100 to 200 GPa and a tensile strength of 4.9−7.5 GPa in its crystalline form,[48,49] cellulose has established itself as a promising material for engineering applications, especially under windy weather in extreme Arctic conditions. We designed a three-layer cooling geotextile consisting of a robust woven biomass scaffold, a permeable and opaque nonwoven cotton fiber layer, and a high-albedo cellulose acetate (CA) coating layer. As the scaffold of the cooling geotextile, the woven biomass scaffold with the modified topological weave pattern (Figure 2a, left) is fabricated using natural fibers, such as cotton and jute which are composed of aligned nanofibrils (Figures 2b, S4, and S5). A network of entangled cellulose fibers with a diameter of 13.5 $\mu$m ± 5.7 $\mu$m (Figure S6) is then laminated onto the woven biomass scaffold by needle punching without the need for additional chemical adhesives (Figure 2a, middle).[50,51] The jute and cellulose fibers intertwine (Figure 2c), providing a robust structure for geotextile applications. CA is then coated on the fibers to form the cooling geotextile (Figure 2a, right) after the solvent quenching process,[52] which yields a wide pore size distribution from 100 to 4000 nm (Figure 2d, and described in the Materials and Methods section). During the solvent quenching of CA coating, the acetone (solvent) rapidly evaporates, causing the CA to phase-separate from the ethanol (nonsolvent) and form nano- and micropores after the evaporation of ethanol.

The ability to upscale fabrication cost-effectively is a prerequisite to protecting thawing Arctic permafrost. A 100 m long and 1.0 m wide laminated scaffold composed of woven jute scaffold and a nonwoven cotton fiber layer has been manufactured (Figures 2e and S7−S10, and SI Section 2). Uniform arrays of punching needles are applied to entangle and bind the woven and nonwoven fiber layers together, producing a robust laminated jute scaffold. Figure 2f demonstrates a large-scale deployment of a cooling geotextile on bare ground. The low carbon footprint (∼0.7 $kg{\cdot}m^{-2}$) makes it an environmentally sustainable alternative for geoengineering applications in vulnerable permafrost regions (SI Section 3). Moreover, life cycle analysis indicates that the cooling geotextile has a reduced impact on climate change, fossil depletion, and chemical and energy consumption compared to the conventional polyurea foam (Figures S11 and S12).

Given the reported extreme coldness (which can drop below −50 °C in Alaska), the freeze−thaw cycles of bare ground, the melting of ice and snow, and sharp rocks in the Arctic region, a need for a mechanically robust approach to mitigate the permafrost thawing and reinforce coastline cannot be overstated. Our cooling geotextile is qualified and even exceeds the mechanical strength and permittivity requirements of geotextile according to the National Engineering Handbook (NEH) (Table S2 and SI Section 4) because of the hierarchically physical entanglement at nano- and microscales and hydrogen bonding at the molecular level. As illustrated in Figure 2g, the cotton-based and jute-based cooling geotextiles exhibit higher tensile strengths of 1029 and 1,682 kg than the NEH requirement of 112 kg. The tensile strains at the point of failure for cotton-based and jute-based cooling geotextiles both fall below 50%, meeting the criteria outlined in the NEH. In addition, the tensile strength of the cooling geotextile is retained over 95% after undergoing freeze−thaw cycles (Figure S13), demonstrating good durability in humid and cold climates. The trapezoidal tear strengths of the cotton-based and jute-based cooling geotextiles are 149 and 191 kg, respectively, which far exceed the NEH requirement of 50.8 kg (Figure 2h). Moreover, the cotton-based and jute-based cooling geotextile can withstand 56.5 and 61.0 kg puncture strength, respectively, which meets the NEH puncture strength requirement of 40.8 kg (Figure 2i). This makes it mechanically strong enough to withstand the sharp surfaces of rocks, roots, sticks, or other debris and trampling by wildlife in the Arctic. Notably, even when subjected to a vehicular load (>1.5 tons), the cooling geotextile remains fully intact with no observable compromise to its structural integrity (Figure S14). The water permittivity of the cotton-based cooling geotextile is measured to be 0.0177 s (Figure S15), indicating that water can flow through ∼28 times faster than the NEH permittivity requirement (0.5 s). This flexible and rollable cooling geotextile (Figure 2j) could effectively prevent flooding formation due to rain during the Arctic summer.

Apart from its reliable mechanical properties, the cooling geotextile is inherently biodegradable (Figures S16−S18 and SI Section 5), which reduces the disposal and long-term environmental remediation cost and protects the sensitive Arctic ecosystem. After 6 weeks in a soil and compost mixture


https://doi.org/10.1021/acsnano.5c06567
ACS Nano 2025, 19, 40774−40788

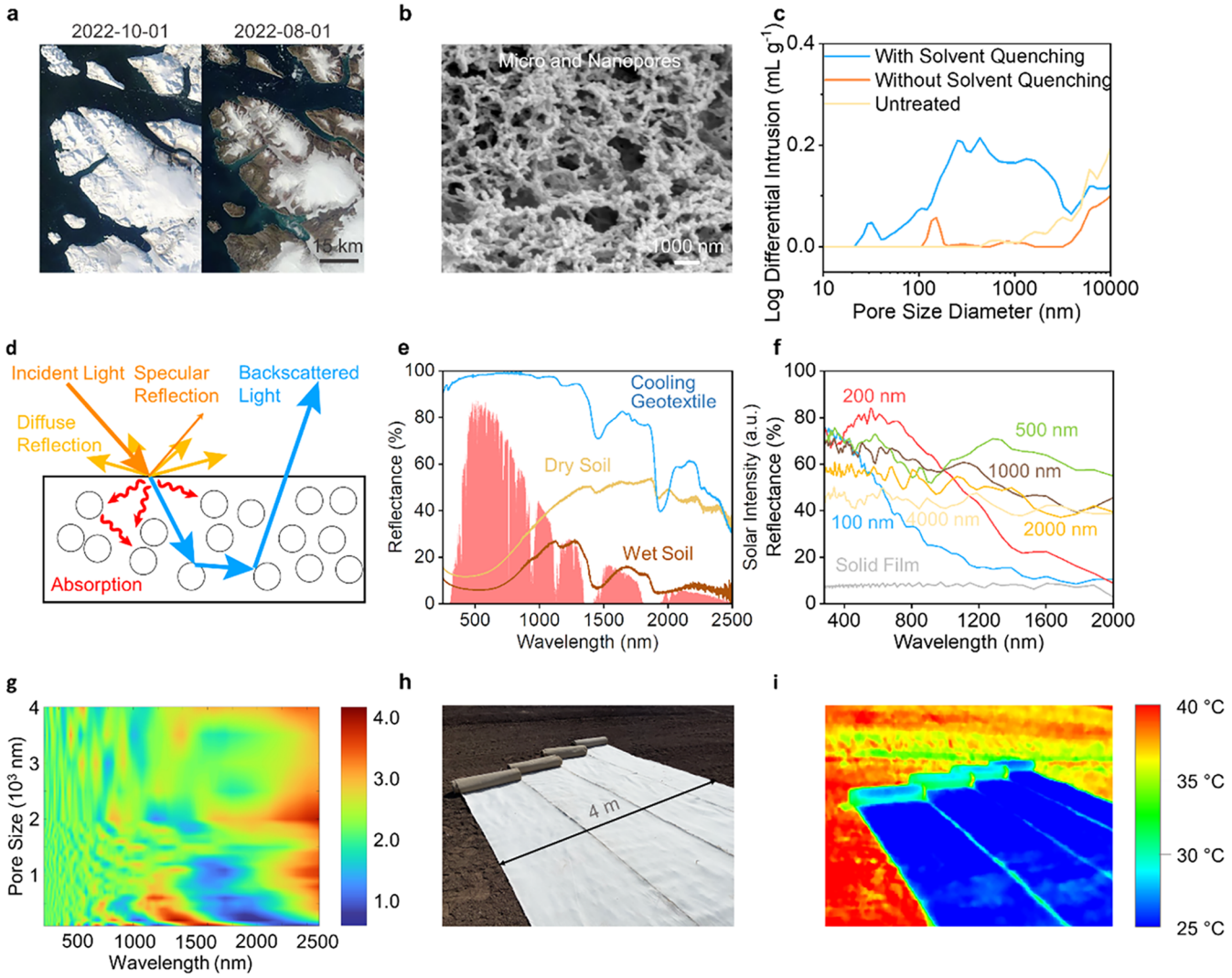


**Figure 3. Albedo engineering of the cooling geotextile. (a) Images of the ground surface covered by snow in October (left) and the exposed bare ground surface in August (right) taken from northwest Greenland near the Thule Air Base (Source: MODIS data). (b) The micro- and nanoscale porous structure of CA after solvent quenching. (c) MIP pore size distribution analysis of cooling geotextile with/without solvent quenching and untreated nonwoven cotton fiber layer. (d) Schematic of the diffused reflection (including backscattering), specular reflection, and absorption on disordered hierarchically porous materials. (e) UV−vis−NIR reflectance spectrum (from 280 to 2500 nm) of cooling geotextile, wet soil (75% water content), and dried soil (0% water content). The red area is the normalized solar irradiance spectrum. (f) FDTD simulated reflectance spectrum for the modeled porous structure of cooling geotextile. (g) FDTD simulated scattering efficiency contour plot for the modeled porous structure of cooling geotextile. (h) The photo and (i) thermographic images of the laminated scaffold rolling over the bare ground. The ambient temperature was ~30 °C.**

with a weight ratio of 1:1 and a water content of 10−50% at 20 °C, the cooling geotextile exhibited a weight loss of over 50 wt % (Figures S19, S20, and SI Section 5), demonstrating the biodegradability of each component in the cooling geotextile. It is important to highlight that the colder average temperatures in the Arctic environment reduce microorganism activity in biodegradation and applying the cooling geotextile on top of the soil limits interactions with subsurface microorganisms. As a result, when our cooling geotextile is deployed directly on the bare ground, its service life is extended due to the slower biodegradation rate in comparison to lab conditions.

Down to the atomic level, cellulose has strong hydrogen bonding between its molecular chains due to the presence of hydroxyl groups in its glucose monomers (Figure 2k, top part). The CA applied to the cooling geotextile has a degree of substitution (DS) of 2.5, meaning that five hydroxyl groups on one glucose unit are substituted by the acetyl groups (Figure 2k, left-bottom part). By using the atomistic model, we investigated interactions at the CA and cotton cellulose interface, while the red arrow indicates the displacement direction (Figure 2k, middle-bottom part). It exhibits that the CA and cotton cellulose can form ~255 hydrogen bonds at a $10 \times 5$ nm$^2$ interface (Figures S22−S25 and SI Section 6). The interfacial energy is 1,650 kcal·mol$^{-1}$ and decreases as the CA is pulled out from the CA and cotton cellulose interface (Figure 2l). The right-bottom part of Figure 2k shows the model for nonequilibrium molecular dynamics, analyzing the mechanical properties of CA and cotton cellulose system (containing 32 chains of CA and 40 chains of cotton cellulose) under compression and tension loading in a vertical direction. The model shows that the tensile strength of CA and the cotton cellulose system is 210 MPa and the compressive


https://doi.org/10.1021/acsnano.5c06567
ACS Nano 2025, 19, 40774−40788

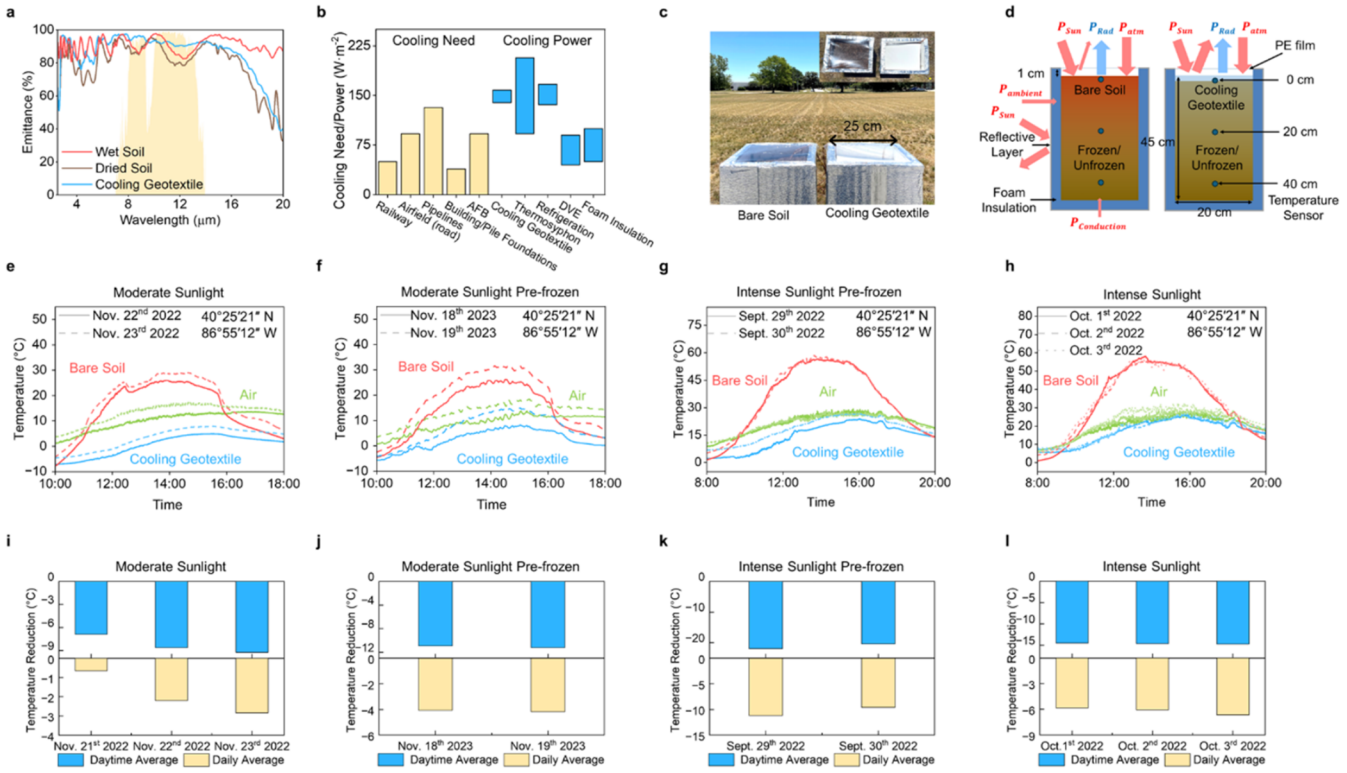


**Figure 4. Heat rejection, thermal load alleviation, and insulation of the cooling geotextile. (a) Emittance spectra (from 2.5 to 20 $\mu$m) of cooling geotextile, wet soil (75 wt % water content), and dried soil (0 wt % water content). (b) Cooling needs for various applications in the Arctic and the cooling power of cooling geotextile and current approaches. (c) Photographs of the setup for the field test under sunlight. The prefrozen/unfrozen soil depth is 45 cm to simulate the properties of natural permafrost, and it was surrounded by thermal-insulated foams to reduce heat transfer with the ambient. (d) Schematic of the heat transfer process for the field test setup with the cooling geotextile and the bare soil. (e–h) Real-time temperature data for unfrozen and prefrozen soil samples under moderate (solar radiation up to ~500 W·m$^{-2}$) and intense (solar radiation up to ~700 W·m$^{-2}$) sunlight. (i–l) Daytime and daily average soil temperature reductions for unfrozen and prefrozen soil under moderate and intense sunlight.**

strength is 280 MPa, respectively (Figure 2m). As suggested by the atomic-level interaction of CA and cotton cellulose chains, physical entanglement among the three layers, and woven pattern of biomass scaffold, the cooling geotextile features a higher grab tensile strength (970 kg) compared to the original woven cotton scaffold (938 kg) and the laminated cotton scaffold (953 kg) (Figure S26).

**Albedo Engineering via Compositional and Structural Modifications for Heat Rejection.** Solar radiation is one of the major thermal loads of permafrost thawing in low-albedo regions where the ground surface substantially absorbs solar radiation, warming the active layer and transferring heat to the permafrost layer underneath. Among the natural substances with different albedo in the Arctic, fresh snow features the highest albedo value (typically 80–90%) to effectively reflect solar radiation, reducing the heating effect on the soil underneath.[53,54] However, during the Arctic summer, diminished snow cover exposes low-albedo bare ground, substantially increasing the absorption of solar energy. This can be seen from the distinguished morphology change of the Arctic bare ground during winter and summer in Figure 3a.[55]

Cellulose features a low absorption (<7%) in the solar range;[56] however, pristine woven cotton scaffold and laminated cotton scaffold show solar reflectance of 72.2 and 82.6% (Figure S27) owing to the presence of other substances such as waxes, protein, and pectin, as well as the large pores inside (≤100 $\mu$m). Additionally, due to the loose entanglement of cellulose microfibers, the nonwoven cotton fiber layer (600 $\mu$m) exhibits a solar transmittance of ~17%, resulting in a solar reflectance of ~76% (Figure S28). The solvent quenching process in the CA coating layer effectively increases the submicron pores up to 0.2 mL·g$^{-1}$ and yields a nano- and micropore size distribution from 100 to 4000 nm compared with that of nonwoven fabrics (from 1 to 10 $\mu$m), as indicated by the SEM image (Figures 3b and S29) and mercury intrusion porosimetry (MIP) analysis (Figure 3c). The size and distribution of those pores can be tuned by varying the solvent choices, CA concentration, and drying conditions to optimize their albedo (Figure S30 and described in the Materials and Methods section). Moreover, CA is produced by modifying cellulose through acetylation, in which acetyl groups are added to the cellulose molecule. These introduced acetyl groups decrease the crystallinity of cellulose[57] and reduce the propensity to photooxidation,[58,59] providing CA with a lower absorption over UV and visible wavelengths compared with cellulose (Figure S31). Therefore, as an effective backscattering medium of sunlight, those hierarchical pores of the CA coating layer can further enhance the solar reflectance of the cooling geotextile (Figures 3d, S32, and S33). A maximized albedo of 96.3% of cooling geotextiles was achieved by a relatively low thickness of ~100 $\mu$m CA coating on top of the nonwoven fiber layer, as indicated by the reflectance spectra in Figure 3e. This thickness is much thinner than other radiative cooling


https://doi.org/10.1021/acsnano.5c06567
ACS Nano 2025, 19, 40774–40788

films (>500 $\mu$m) fabricated by the solvent quenching method.[60]

To understand the underlying mechanism, we used a finite-difference time-domain (FDTD) method to simulate the reflectance spectra and scattering efficiency of the modeled porous cooling geotextile (Figures 3f,3g and S34). As MIP results indicate a wide pore size distribution from 100 to 4000 nm in the cooling geotextile, where the sizes of submicron pores are mainly around 100, 200, and 500 nm, we selected these nanopore sizes and micropores (1000, 2000, and 4000 nm) for the simulation. The results illustrate that nanopores effectively reflect visible sunlight (≤80%) with scattering efficiencies up to ∼4. The micropores demonstrate effective reflection (>40%) in the NIR range with scattering efficiencies over 3 (Figure S35). In addition, the simulated CA film yields a low absorption in the solar range, which correlates with the experimentally measured solar absorption of 2% (Figure S32). Considering that the pore size distribution of cooling geotextile ranges from 100 to 4000 nm induced by the solvent quenching process, its high solar reflectance mainly results from the hierarchically porous fiber network and CA coating layer.

Taking advantage of the low solar absorption and high diffuse reflection of the CA layer (Figure S36 and SI Section 7), the cooling geotextile possesses a high solar reflectance of 96.3% from 250 to 2000 nm (Figure 3e). In contrast, the wet soil sample and dry soil sample display a low solar reflectance of 16 and 29% due to their elevated ratio of the absorption coefficient and scattering coefficient (Figure S36). To better understand solar heating effects in the Arctic environments, the soil heating power is estimated for soils with different water contents (SI Section 8). Under AM 1.5 solar irradiance, the solar heating power of soil increases from 600 to 750 W·m$^{-2}$ when the water content rises from 0 to 75 wt % (Figure S38). This suggests that the soil with a higher water content tends to absorb more solar energy to heat the permafrost layer during summer. Considering that the Arctic summer radiation is lower than the AM 1.5 solar irradiance, the Arctic soil heating power is scaled to 279−546 W·m$^{-2}$ based on latitude. After being covered by our cooling geotextile, the surface albedo will be substantially increased from 30 to 96.3%, as shown by the comparative albedo analysis of different Arctic natural substances (Figure S39).[31−35] Among these natural substances on ground level, Arctic vegetation (8−32%), soil (10−30%), and ice (30−40%) all have relatively low albedo. Their solar reflectances fluctuate widely for different species and different seasons. Snow albedo decreases when impurities, such as dust and sand, are introduced, and it varies across different seasons.[61] As the cloud fraction and density decrease, fewer clouds are available to reflect sunlight. Consequently, more sunlight reaches the ground, leading to increased absorption and resulting in a reduction in the overall cloud albedo. Conversely, the cooling geotextile has a constant albedo of 96.3%, independent of seasonal changes, ensuring a reliable heat rejection effect. To visualize the heat rejection effect, four rolls of laminated scaffold (4 m wide) were placed over the soil for half an hour under direct sunlight (Figure 3h), and a thermal image was taken to show the temperature distribution (Figure 3i). The cooling geotextile was observed to be ∼15 °C cooler than that of the bare soil.

**Soil Cooling Performance in Field Tests via Heat Rejection and Heat Extraction.** The heat rejection capacity of the cooling geotextile is validated by its high albedo, which effectively minimizes solar absorption during the day by reflecting solar radiation. Another key feature of cooling geotextile is the high thermal emittance of 93% over the atmospheric window from 8 to 13 $\mu$m, allowing for efficient radiative heat dissipation to the cold outer space (Figure 4a). This high thermal emittance stems from the strong molecular vibrations including O−H, C ═ O, C−H, C−O, and C−O−C of CA and cellulose in cooling geotextile (Figure S40).[56,62] Based on the measured thermal emittance spectra (2.5−20 $\mu$m), the daytime cooling/heating powers of soil and cooling geotextile are evaluated (SI Section 8). The daytime heating powers of soil are 407−609 and 285−369 W·m$^{-2}$ under AM 1.5 and Arctic summer conditions, respectively (Figure S41). On the contrary, the cooling geotextile exhibits a cooling effect, achieving a cooling power of 139 W·m$^{-2}$ under AM 1.5 and 158 W·m$^{-2}$ during the Arctic summer. Therefore, the surface of the cooling geotextile will be self-cooled below ambient temperature, even in the Arctic summer, which can effectively cool the soil. In addition, effective cooling technologies are essential to meet various Arctic cooling needs (Figure 4b), including transportation, infrastructure foundation, and artificial frozen barriers (AFB). For example, the cooling load of railways is estimated to be 50 W·m$^{-1}$ for stabilizing its embankment and resisting ambient heating.[63] Roads and airfields without embankments for enhanced air convection cooling require at least 92 W·m$^{-2}$ of cooling power to counteract the heating from solar and ambient.[26] Furthermore, a 132 W·m$^{-2}$ cooling power is needed to protect the permafrost underneath the pipelines, offsetting heat flux from pipelines and heated ground.[64] To stabilize the building and pile foundation, an ∼39 W·m$^{-2}$ cooling power is required to mitigate the downward heating from structures.[65] AFB, which needs a cooling power of 92 W·m$^{-2}$, similar to that of roads, acts as a solid and impermeable layer that prevents the movement of groundwater to avoid the release of hazardous substances and maintains the integrity of structures built on or near permafrost.[66] A comprehensive performance comparison has been conducted and is detailed in Table S7. The duct-ventilated embankments (DVE) (45−90 W·m$^{-2}$)[67] and foam insulation (50−100 W·m$^{-2}$)[21] can only meet the cooling needs for transportation and building foundation. However, they might fail under hotter conditions, where greater heat dissipation is required. While thermosyphon and refrigeration systems provide comparable cooling powers (92−207[26] and 136−167 W·m$^{-2}$,[68] respectively), they require a high installation cost and refrigeration systems demand continuous energy input. In contrast, the cooling geotextile delivers competitive cooling performance at significantly lower cost, weight, and environmental impact without requiring external energy input.

To further validate its viability, a one-dimensional heat transfer analysis (SI Section 8) is carried out to analyze the energy balance of bare soil and soil covered with cooling geotextile, considering both radiative cooling power and sensible heat. The one-dimensional energy balance analysis results demonstrate that the cooling geotextile substantially reduces the soil temperature. Specifically, the soil covered with cooling geotextile is over 30 °C cooler than the bare soil and 8 °C cooler than the air temperature (Figure S42). These findings highlight the priority of employing the cooling geotextile as an efficient cooling solution for soil surfaces. Moreover, the micro- and nanosized structures in cooling geotextile reduce the phonon pathways and impede air molecular movements during the heat transfer, resulting in a


https://doi.org/10.1021/acsnano.5c06567
ACS Nano 2025, 19, 40774−40788

notably low thermal conductivity.[69,70] This low thermal conductivity of the cooling geotextile (0.028 $W{\cdot}m^{-1}{\cdot}K^{-1}$) makes it an effective thermal barrier between the ambient and soil, further inhibiting the temperature rise during the Arctic summer.

To experimentally demonstrate the performance of cooling geotextile, field tests were conducted to record the temperature response of the bare soil and soil covered by cooling geotextile at Purdue University, West Lafayette, IN (40°25′21″ N, 86°55′12″ W) (SI Section 9). As shown in Figure 4c, two insulation boxes with the same soil were wrapped in aluminum foil, with one side facing the sky. The insulation box can effectively resist heat flux from ambient and heat conduction from the bottom (Figure 4d). The wrapped aluminum foil can reject solar radiation to avoid heating the insulation box. One group was covered with cooling geotextile, while the other was only the bare soil. A 20 $\mu$m thick polyethylene film, transparent to both solar and infrared wavelengths, was employed as a convection cover to reduce convective heat transfer and prevent heat accumulation.[56,71] Since the film is transparent to mid-infrared radiation, the blackbody emission from the soil can readily radiate outward without being trapped, preventing heat buildup. Additionally, the air gap between the soil surface and the polyethylene film is maintained at 1 cm to further minimize heat accumulation, which is common in greenhouses. Temperature sensors were inserted in the soil at depths of 0, 20, and 40 cm, respectively, for temperature measurement (Figure 4e–l). Figure 4e shows the surface temperatures of bare soil and cooling geotextile-covered soil over two consecutive days under natural sunlight. We intentionally selected field test days with an average ambient temperature of ∼ 10 °C and moderate sunlight (maximum solar intensity of ∼500 $W{\cdot}m^{-2}$) (Nov. 22nd to Nov. 23rd, 2022), as these conditions closely match the average temperature and solar irradiation of the Arctic summer. The average daytime soil temperature reductions were 8.6 and 9.2 °C on these 2 days when the soil was covered with a cooling geotextile (Figure 4i). In contrast, the bare soil, with its low albedo, exhibited a rapid temperature increase in response to fluctuations in solar irradiation, leading to a substantial temperature increase as the solar intensity increased from 200 to 500 $W{\cdot}m^{-2}$ (Figures S43 and S44). Surface temperature rise also led to the quick temperature increase of soil at depths of 20 and 40 cm. Moreover, we found that the daily soil temperature reduction (∼2 °C) is lower than the daytime temperature reduction, as the daily average includes nighttime temperatures. This difference can be attributed to the radiative cooling effect of soil during the night. With its measured emittance ranging from 0.86 to 0.90, the soil releases heat through radiation during the night, which lowers the overall daily temperature reduction. In addition, field tests were conducted with the prefrozen soil samples to mimic the permafrost thawing process in Arctic summer (Figure 4f). The average ambient temperature was approximately 15 °C, with a maximum solar intensity of around 500 $W{\cdot}m^{-2}$ from November 18th to November 19th, 2023. During these 2 days, the cooling geotextile reduced average daytime soil temperatures by ∼11.1 °C and average daily soil temperatures by ∼4.1 °C (Figure 4j), which are greater than the data of unfrozen soil. Given the extensive warming and intense sunlight observed in the Arctic, where daytime temperatures can exceed 20 °C in low-albedo areas, further testing was conducted under higher ambient temperatures and intense sunlight. Specifically, two field tests were performed at ∼ 20 °C ambient temperature of ∼20 °C with a peak solar intensity of ∼700 $W{\cdot}m^{-2}$ (Figures 4g,4h and S45). This solar intensity is comparable to the maximum solar radiation observed during the Arctic summer, as shown in Figure S46, where Barrow (71°18′ N, 156°47′ W) and Kotzebue (66°52′ N, 162°38′ W) reached peak solar radiation of ∼640 and 730 $W{\cdot}m^{-2}$ in one year.[72] The first set of field tests was conducted with prefrozen soil samples from September 29th to 30th, 2022. When exposed to solar radiation, the bare soil surface rapidly heated, and the deeper layers warmed faster compared to those under the cooling geotextile. The temperature of the bare soil increased rapidly from 2 to 17 °C between 8 and 10 am, while the soil covered by geotextile remained near 1 °C during the same period (Figure 4g). During midday, the bare soil was heated up to 55 °C while the surface temperature of the soil covered by geotextile only increased to ∼10 °C, despite an ambient temperature of 20 °C. Compared with the frozen bare soil, the cooling geotextile effectively reduces the average daytime soil temperature by ∼21 °C and the average daily soil temperature by ∼10 °C (Figure 4k). The cooling geotextile not only effectively rejected the solar heating but also reduced the heat transfer from the surrounding environment with a low thermal conductivity of 0.028 $W{\cdot}m^{-1}{\cdot}K^{-1}$ (Figure S48). The cooling geotextile, as a thermal insulation layer, has the potential to protect permafrost from thawing under high ambient temperatures. The second set of the field test was conducted with soil samples without prefreezing, from October 1 to October 3, 2022. As the solar intensity peaks, the surface temperature of bare soil (∼58 °C) is ∼33 °C higher than that of cooling geotextile-covered bare soil (∼25 °C) (Figure 4h). The cooling geotextile consistently reduced the temperatures of bare soil by an average of 14.6 °C during the daytime and 6.2 °C over a full 24 h period (Figure 4l). We find that the average daytime and daily temperature reductions are greater when the soil samples are prefrozen and the sunlight is intense. This indicates that cooling geotextile is particularly well suited for protecting permafrost or frozen soil and that its cooling performance could be enhanced during the Arctic summer, when solar radiation is stronger.

Evaporative cooling is another advantage of our cooling geotextile. Cellulose fiber layers have the property of absorbing water from either air or soil (SI Section 10). Specifically, the cellulose fiber layer demonstrates the capacity to absorb a range of 1.2 to 10 wt % of water from air characterized by relative humidity levels spanning from 20 to 80%, as well as 20 to 29 wt % of water when it is placed over the soil with a relative humidity ranging from 20 to 40% (Figure S49 and SI Section 10). Assuming deployment of the cooling geotextile over the soil with a moisture content of 20 wt %, it has the potential to absorb approximately 20 wt % of water from the soil and subsequently release this moisture through evaporation into the atmosphere. This theoretical estimation of evaporative cooling power stands at 38–151 $W{\cdot}m^{-2}$ for cotton cellulose with a water content of 20 wt %, as illustrated in Figure S50. To protect thawing permafrost under real Arctic conditions, we secured the cooling geotextile with wooden stakes spaced 1 m apart, as shown in Figure S51—a common method used for geotextile applications in soil reinforcement. A ∼1.5 cm thick air gap was observed near the edge of the cooling geotextile when the maximum wind gust speed was recorded as 7 $m{\cdot}s^{-1}$. As the wooden stakes applied tension to the secured cooling geotextile, most parts of the cooling


https://doi.org/10.1021/acsnano.5c06567
ACS Nano 2025, 19, 40774–40788

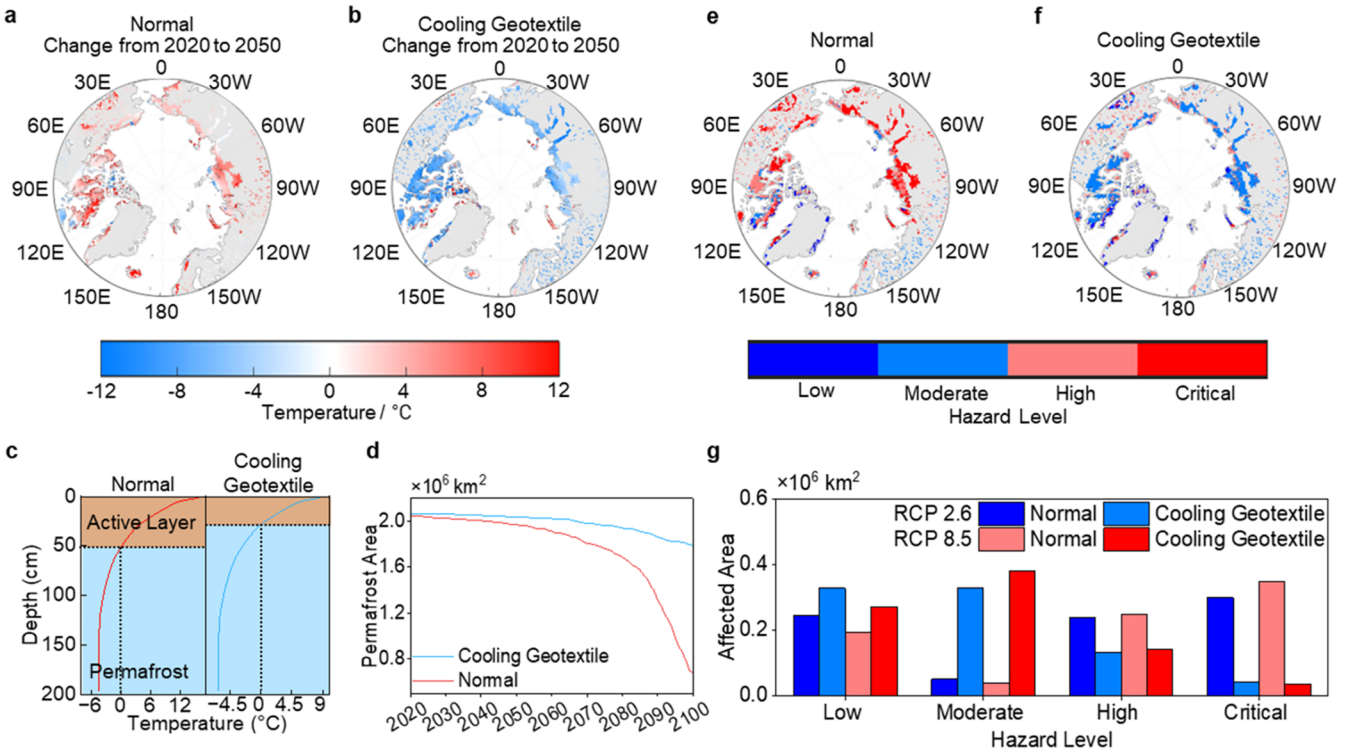


**Figure 5. Simulation of permafrost thawing prevention via the cooling geotextile and the hazard risk assessment under the RCP 8.5 scenario. (a, b) Predicted soil temperature change from 2020 to 2050 without and with cooling geotextile. (c) Soil temperature profile in 2050 under the RCP 2.6 scenario without and with cooling geotextile. (d) Estimated permafrost area changes from 2020 to 2100. (e, f) Pan-Arctic infrastructure hazard map without or with a cooling geotextile. (g) Affected area at different classified hazard levels: low (1), moderate (2), high (3), and critical (4).**

geotextile remained static under the wind. The flexibility of the geotextile enables its secure installation on uneven terrain, providing an effective stabilization against Arctic winds. An aerodynamic simulation shows that the air gap between the geotextile and the ground remains below 2.2 cm under typical Arctic summer wind speeds (5−7 $m \cdot s^{-1}$) (Figures S52, S53, and SI Section 11).

**Simulation of Temperature Profiles and Hazard Risk Assessment for the Arctic Bare Ground and Relevant Permafrost Areas.** To forecast the long-term benefits of large-scale implementation of the cooling geotextile at protecting permafrost, we incorporate a soil thermal model (STM) into a Lund−Potsdam−Jena (LPJ) Dynamic Global Vegetation Model[73−76] (SI Section 12). It is important to note that while our model simulates the entire Arctic bare ground to assess the potential global impacts of the cooling geotextile, it is intended as a proof-of-concept to quantify the maximum benefits and reductions in hazard risk. In practice, the cooling geotextile is targeted for localized application in areas susceptible to permafrost degradation and land subsidence (e.g., those impacted by infrastructure disturbances, thermo-karst formation, thermal erosion, and detachment slides). Large-scale vegetation distribution, soil thermal regime, and carbon cycling are modeled with a horizontal resolution of 0.5° × 0.5°. The real-time temperatures collected in field tests are used to calibrate the pan-Arctic soil surface temperature profile simulation from 2000 to 2100. Two emission scenarios are considered: Representative Concentration Pathway (RCP) values of 2.6 and RCP 8.5. RCP 2.6 is a stringent pathway that could maintain global temperature rise below 2 °C by 2100.[77] RCP 8.5 is generally considered a high-emission scenario, where emissions continue rising throughout the 21st century.

The simulated soil surface temperature changes in the Arctic region from 2020 to 2050 under RCP 2.6 and RCP 8.5 scenarios with and without a cooling geotextile are shown in Figures 5A,B and S54. In the absence of cooling geotextile, the average surface temperature rise of the bare surface is 1.11 °C under the RCP 2.6 scenario (Figure S54), while the warming is more pronounced under the RCP 8.5 scenario (Figure 5a), characterizing a temperature increase by 2.85 °C in even larger areas than RCP 2.6.[78] This indicates that under the RCP 8.5 scenario, the Arctic region will experience more significant warming without any protection on bare ground, which could yield far-reaching consequences for global climate change, underscoring the pressing need for the implementation of our cooling geotextile. The modeling results (Figures 5b and S54) also reveal the effective cooling performance of the cooling geotextile in the vast Arctic, exemplified by a temperature reduction of up to 12 °C. Under the RCP 2.6 scenario, the cooling effects are distinct in Northern Russia and Northern Europe, followed by Northern Canada and Alaska, resulting in an average temperature reduction of 4.3 °C over the bare ground. For the RCP 8.5 scenario, our cooling geotextile results in an average temperature reduction of 5.78 °C over the bare ground in 2020. Notably, from 2050 to 2100, the average surface temperature of the Arctic bare ground increases from 0.01 to 1.76 °C under RCP 2.6 and from 3.77 to 12.64 °C under RCP 8.5. But in 2100, the cooling geotextile-covered bare ground remains −2.92 °C under RCP 2.6 and increases from −2.01 to 4.09 °C under RCP 8.5 (Figures S55 and S56).


https://doi.org/10.1021/acsnano.5c06567
ACS Nano 2025, 19, 40774−40788

Apart from the soil surface temperature, near-surface permafrost content (0−2 m) is investigated by simulating the vertical soil temperature profiles at 70° N, 154° W (Northern Alaska) with or without cooling geotextile under the RCP 2.6 scenario (Figure S54) and RCP 8.5 scenario (Figures 5c and S57). The simulation shows that the cooling geotextile could preserve the permafrost layer by 20.5 cm in 2050 under an RCP of 2.6 (Figure S54) and 23 cm at RCP 8.5 (Figure 5c), respectively. Under the RCP 2.6 scenario, the depth of the active layer for cooling geotextile-protected permafrost is around 25 cm, while the depth of unprotected permafrost will fluctuate around 44 cm from 2050 to 2090 (Figure S54). Under the RCP 8.5 scenario, the increased air-soil temperature gradient drives substantial amounts of heat into the soil, resulting in dramatic thawing of unprotected permafrost from 2060 to 2090, and the active layer can reach beyond 200 cm in 2090 (Figure S57). With engineered solar albedo, radiative cooling, and thermal insulation, the cooling geotextile can overcome the increased air-soil temperature gradient and preserve 91 cm of permafrost by 2090. Assuming that the Arctic permafrost at 70° N, 154° W stocks 35.5−86.2 $kg{\cdot}m^{-3}$ of organic carbon,[79] the cooling geotextile can reduce the potential permafrost carbon release by 7.28−17.67 $kg{\cdot}m^{-2}$ under RCP 2.6 and 8.17−19.83 $kg{\cdot}m^{-2}$ under RCP 8.5 from 2020 to 2050. In addition, the effect of the air layer is considered in the applied global model (SI Section 12). During a large-scale deployment of the cooling geotextile, due to the unevenness of the bare ground, about a 1 cm thick air layer can form between the cooling geotextile and ground under wind at a speed of 5 $m{\cdot}s^{-1}$, based on the fluid dynamic simulation (SI Section 11). This air layer can further reduce the heating effect from the ambient air. Air with a low thermal conductivity of 0.024 $W{\cdot}m^{-1}{\cdot}K^{-1}$ at 0 °C shows an insulation effect in the global model (Figure S59 and SI Section 12).

Quantitative area forecasts of permafrost with a depth from 0 to 2 m show that, without the use of cooling geotextiles, the permafrost area will decrease by 49,000 and 65,000 $km^2$, respectively, under RCP 2.6 and RCP 8.5 scenarios from 2020 to 2050 (Figures 5d and S54). On the contrary, with cooling geotextile, the permafrost area will be preserved by 27,000 and 40,000 $km^2$ under RCP 2.6 and RCP 8.5 scenarios, respectively, compared to bare ground in 2050. In 2050, the cooling geotextile is estimated to mitigate the permafrost carbon emission by 58.6 $kg{\cdot}m^{-2}$ under the RCP 8.5, which indicates that ∼2.336 Pg carbon emission can be avoided by 2050. Notably, from 2050 to 2100 under the RCP 2.6 scenario, the uncovered permafrost area would decrease from 2.007 to 1.968 million $km^2$, while the cooling geotextile-covered permafrost area would decrease to 2.028 million $km^2$ permafrost. Furthermore, under the RCP 8.5 scenario, the uncovered permafrost area is projected to decline to 0.979 million $km^2$ in 2100 while cooling geotextile-covered bare ground could still maintain 1.792 million $km^2$ permafrost.

To better understand the infrastructure hazard risk due to permafrost thaw, we employ an analytic hierarchy model to define a hazard index that incorporates important factors such as active layer thickness, ground ice content, ground temperature, fine-grained sediment content in the ground, and slope gradient.[80−82] Active layer thickness and ground temperature are derived from our global model. The ground ice content, fine-grained sediment content in the ground, and slope gradient are obtained from publicly available data sources.[83−85] These factors are then classified into four categories based on their impact on the permafrost thawing-related infrastructure hazard (4 = critical hazard, 3 = high hazard, 2 = moderate hazard, 1 = low hazard).[86] We have generated pan-Arctic infrastructure hazard maps under RCP 2.6 and RCP 8.5 in 2050 (Figures 5e,f and S58). The simulated infrastructure hazard maps indicate that more than half of the bare ground area over Arctic permafrost will be at high and critical hazard levels, posing risks to pipelines, roads, railways, airports, settlements, and industrial areas. For instance, the Trans-Alaska Pipeline System in the United States, gas pipelines in the Yamal-Nenets region of Russia, and the Obskaya-Bovanenkovo railway are projected to be at high or critical hazard risk without the cooling geotextile by 2050 under both RCP 2.6 and 8.5 scenarios. Notably, under RCP 8.5, about 60,000 $km^2$ more bare ground is classified as being at high and critical hazard risk compared to RCP 2.6, due to the increase associated with RCP 8.5. In contrast, our cooling geotextile can be applied to lower the hazard risk from high/critical to low/moderate level. Specifically, the cooling geotextile effectively reduces the high and critical hazard area from 0.54 million $km^2$ to 0.18 million $km^2$ under RCP 2.6 and from 0.60 million $km^2$ to 0.18 million $km^2$ under RCP 8.5 (Figure 5g), contributing to the stabilization of the landscape and affected infrastructure.

Current permafrost thawing processes can be categorized into gradual thaw, releasing 613−802 tetragram carbon per year ($TgC{\cdot}yr^{-1}$), and abrupt thaw, emitting 624−960 $TgC{\cdot}yr^{-1}$[87] (Figure S61). Gradual thaw occurs beneath polar deserts, tundra, vegetated areas, and wetlands, while abrupt thaw involves dramatic terrain changes, such as the formation of thermokarst lakes, collapsed scar wetlands, slumps, and gullies.[88] Specifically, polar deserts absorb substantial solar heat, leading to $CO_2$ emissions ranging from 5 to 297 $TgC{\cdot}yr^{-1}$ (depending on the soil organic matter in the active layer).[89,90] Tundra, a treeless Arctic plain covered with bare/rocky ground or vegetation, disperses 238 $TgC{\cdot}yr^{-1}$ of $CO_2$ and $CH_4$ into the atmosphere.[88] Thermokarst lakes (14−18 $TgC{\cdot}yr^{-1}$) and wetlands (32−38 $TgCH_4{\cdot}yr^{-1}$)[91] are major sources of $CH_4$ through ebullition and aerenchymous transference. Additionally, Arctic wildfires cause abrupt $CO_2$ releases of 57−408 $TgC{\cdot}yr^{-1}$.[92] While the boreal forest acts as a carbon sink, capturing 992 $TgC{\cdot}yr^{-1}$ through $CO_2$ absorption via photosynthesis and $CH_4$ oxidation by methanotrophic microorganisms,[93] it is insufficient to offset the carbon emissions from permafrost thawing (potential net carbon emission ≥245 $TgC{\cdot}yr^{-1}$). Notably, our cooling geotextile has the potential to reduce carbon emissions by 78 $TgC{\cdot}yr^{-1}$ under the RCP 8.5 scenario by 2050 (SI Section 12). Our modeling results highlight that the deployment of cooling geotextile is effective for cooling Arctic bare ground with a temperature reduction of ∼5.78 °C from 2020 to 2050, preserving 40,000 $km^2$ of permafrost, lowering the hazard potential for infrastructures, buildings, and landscapes, and reducing ∼32% of the potential net carbon emissions.

## CONCLUSIONS

Thawing permafrost radically reshapes the Arctic landscape and releases pulses of carbon into the atmosphere. Facing those challenges, our work demonstrates an achievable and easy-to-retrofit approach to cool permafrost and stabilize landscapes via a sustainable, biodegradable, and scalable cooling geotextile that can be deployed over low-albedo areas relevant to intense human activities, energy infra-


https://doi.org/10.1021/acsnano.5c06567
ACS Nano 2025, 19, 40774−40788

structures, and natural disturbances, including buildings, shorelines, thermokarst, and sinking landscapes in the Arctic. Benefiting from the unique optothermal structure derived from its hierarchical structures and attributes of cellulose-based materials, the cooling geotextile cools down and even recovers the permafrost by boosting the albedo up to 96.3%. The strong scattering of sunlight by hierarchical cellulose fibers and micro- and nanosized pores enables efficient solar heating rejection, while molecular vibration of chemical bonds in cellulose materials facilitates radiative cooling by enhanced thermal emittance. This dual mechanism minimizes the thermal load on soil from solar heating during Arctic summer, characterized by a daytime cooling power of 139 $W{\cdot}m^{-2}$. In addition, the low thermal conductivity of cooling geotextiles resulting from their porous structures contributes to the inhibition of heat exchange between the soil active layers above permafrost and the warming air, thus further reducing the temperature throughout varying seasons. Assisted by its mechanical robustness, the cooling geotextile can withstand the prevalent environmental rigors inherent to the Arctic settings, broadening its applications for soil reinforcement, ground stabilization, and erosion control in geoengineering scenarios. The roll-to-roll manufacturing of a cooling geotextile expedites large-scale fabrications, and its rollable feature enables its facile implementation. The global model simulations show that the cooling geotextile can reduce the Arctic bare ground temperature by up to 12 °C during summer from 2020 to 2050, securing the permafrost preservation of over 20 cm depth at 70° N,154° W (Northern Alaska). Furthermore, 40,000 $km^2$ of permafrost area is estimated to be preserved after being covered by cooling geotextile, and at least 2.336 Pg carbon emissions can be avoided. Distinguished by its reliable cooling potential, biodegradability, and scale-up fabrication, the cooling geotextile establishes itself as a promising bridge toward carbon neutrality in 2050.

## MATERIALS AND METHODS

**Preparation of the Cooling Geotextile.** Cooling geotextile comprises a woven biomass scaffold, a nonwoven cotton fiber layer, and a cellulose acetate (CA) coating from the bottom to the top layers. The woven biomass scaffold is made by weaving engineered strings from natural fibers with optimal topological pattern. Nonwoven cotton fiber layer is produced from 100% raw cotton (purchased from *Alibaba*). After raw cotton goes through the carding and webbing process, it forms a cotton web. The cotton web is then further hydroentangled to produce the nonwoven cotton fiber layer. The nonwoven cotton fiber layer is laminated onto the woven biomass scaffold by a needle punching process.

To create an effective solar reflection surface, CA (Degree of Substitution (DS) = 2.5, Thermo Fisher Scientific, Mw = 100,000) was first dissolved in acetone (Thermo Fisher Scientific, ACS reagent) and stirred overnight to form a transparent solution. Then, methanol (Thermo Fisher Scientific, Environmental grade) was added to the CA solution with a 3:5 weight ratio to acetone. The precursor solution was then dropped and cast onto the nonwoven cotton fiber layer surface over the biomass-woven scaffold and left to air-dry. The samples without solvent quenching were drop-cast with a CA solution without methanol. In addition, we have applied Nuclear Magnetic Resonance (NMR) to measure the chemical shift and peak intensity of CA. From the $^1H$ NMR result (Figure S62), we can obtain the peak area of $-COCH_3$ group (7.85) and H3 (1.03). Thus, the DS value is calculated to be **2.54** based on the following equation:

$$DS = \frac{\text{intensity}(COCH_3)}{3 \times \text{intensity}(H_3)}$$

**Preparation of the CA Film with/without Solvent Quenching.** The solution containing CA in acetone is drop-cast onto a clean glass slide and dried overnight, yielding a pure CA film without solvent quenching. In contrast, the solvent-quenched CA film is produced by drop-casting a mixture of CA, acetone, and methanol. The formed CA film is measured to have a thickness of ∼100 $\mu$m.

**Tensile Strength Test.** The tensile test data of the woven biomass scaffold, nonwoven cotton fiber layer, CA films, and cooling geotextile were collected via Mechanical Testing Systems (MTS Criterion Series 40 Electromechanical Universal Test Systems). The test was performed with the upper fixture moving upward at a constant velocity of 300 $mm{\cdot}min^{-1}$.

**Optical Characterization.** Ultraviolet, visible, and near-IR spectral reflectance and transmittance of CA, nonwoven cotton fiber layer, cooling geotextile, soils, and other materials were obtained by Lambda 950 (200−2500 nm wavelength). The diffuse reflection is measured by removing the specular exclusion port on the integration sphere of Lambda 950. The total hemispheric transmittance and reflectance of all the samples (2.5−20 $\mu$m) were measured with ±0.5% uncertainty by a Nicolet iS50 FTIR spectrometer with a PIKE Technologies integrating sphere.

**Calculation of the Overall Solar Reflectance and Thermal Emittance.** The overall hemispherical solar reflectance ($\rho_{eff}$), transmittance ($\tau_{eff}$), and thermal emittance ($\alpha_{eff}$) are functions of wavelength ($\lambda$), which can be expressed as

$$\rho_{eff} = \frac{\int_{0.28\mu m}^{2\mu m} \rho(\lambda) I_{solar} d\lambda}{\int_{0.28\mu m}^{2\mu m} I_{solar} d\lambda}, \quad \tau_{eff} = \frac{\int_{0.28\mu m}^{2\mu m} \tau(\lambda) I_{solar} d\lambda}{\int_{0.28\mu m}^{2\mu m} I_{solar} d\lambda}, \quad \alpha_{eff} = \frac{\int_{2.5\mu m}^{20\mu m} \alpha(\lambda) I_{solar} d\lambda}{\int_{2.5\mu m}^{20\mu m} I_{solar} d\lambda}$$

**Thermal Conductivity Measurement.** A steady-state miniaturized reference bar method was applied to measure the thermal conductivity.[94] The sample was cut to 10 mm by 10 mm and placed between a 'hot side' and a 'cold side'. To obtain precise two-dimensional steady-state temperature maps, an IR camera (QFI MWIR-1024) was used to collect the temperature gradient in the sample region and the actual heat flux (through measurements of the temperature gradient in a known material). The thermal conductivity of the sample could be determined via Fourier's law.

**Imaging and Microscopy.** Images (visible) of the soil, cotton, and cooling geotextile were taken using an iPhone 12 Pro Max. IR images were taken via an FLIR E8-XT. The surface and cross-sectional morphology of the cotton samples, CA films, and cooling geotextiles were characterized by scanning electron microscope (SEM, Thermo Scientific Helios G4 UX Dual Beam).

**Pore Size Distribution.** To determine the nano−micro-structure−property relation in cooling geotextile, we prepared a CA-coated nonwoven cotton fiber layer with or without solvent quenching process and measured the pore size distribution from 0.003 to 1100 $\mu$m via mercury intrusion porosimetry (MIP, AutoPore V 9600, Micromeritics). During the measurement, the controlled pressure was set from 0.2 to 50 psi with a step of 0.05 psi, which allowed the data to be collected in the macropore region. The contact angle between mercury and our samples was taken as 130°.

**Cellulose Content Investigation.** To measure the cellulose content in nonwoven cotton fabric and woven jute fabric, we extracted the cellulose from them by the degreasing and delignification process. The samples were rinsed with toluene, acetone, 2-propanol, and water. Then, the mixture was dried in the oven and weighed. The delignification was performed by immersing the samples in a boiling solution of 2.5 M NaOH and 0.4 M $Na_2SO_3$ for 7 h. Then, the samples are washed with DI water and immersed in a boiling solution of 0.1 M NaOH and 10% $H_2O_2$ for complete delignification. The resulting cellulose fibers were filtered and rinsed with 1 wt % acetic acid, washed with water to neutral pH, dried at 105 °C to constant weight, and weighed to determine cellulose content as


https://doi.org/10.1021/acsnano.5c06567
ACS Nano 2025, 19, 40774−40788

a percentage of the original dry sample mass. The cellulose content was calculated as a percentage of the original dry mass. The cellulose weight fraction was determined to be 90 ± 4% for cotton fabric and 62 ± 3% for jute fabric.

## ASSOCIATED CONTENT

### Supporting Information

The Supporting Information is available free of charge at https://pubs.acs.org/doi/10.1021/acsnano.5c06567.

Potential deployments and geoengineering applications for the Arctic; large-scale manufacturing process; cost analysis, carbon footprint analysis, and life cycle analysis; geotextile requirements and characterizations; soil biodegradation tests; atomistic simulation of hydrogen bonding between CA and cellulose; finite-difference-time-domain simulations; calculation of albedo, heating/cooling power, and surface heat transfer analysis; real-time temperature measurement demonstrations; water absorption of cotton cellulose and theoretical evaporative cooling estimation; air dynamic model of air layer between the ground and the cooling geotextile; LPJ-STM model; photographs of destabilized coastlines and landscapes due to permafrost thawing; satellite images of coastline change; schematics of Arctic coastline erosion; ultimate tensile forces of woven cotton and jute strings and scaffolds; SEM images and fiber width distribution of cotton fibers; large-scale woven jute scaffold fabrication process; nonwoven cotton fiber layer fabrication process; roll-to-roll CA coating process; photograph of a 100 m long cooling geotextile deployed on the grass land; LCA indicators for cooling geotextile and urea foam; tensile strength of the cooling geotextile after freeze−thaw cycles; photograph of mechanical performance under vehicular load; water permittivity under pressure; the cellulose degradation process by cellulase; deacetylation process of CA into cellulose; decomposition of lignin into simpler compounds; biodegradability test of cooling geotextile in soil burial environment; soil burial biodegradation test results; SEM and morphology of CA and cooling geotextile; atomistic simulation models and interfacial energy results; molecular simulations of cotton cellulose water absorption; mechanical comparison of scaffold, laminate scaffold, and cooling geotextile; UV−vis−NIR reflectance spectra of scaffolds and nonwoven cotton; SEM of pure CA film and pore size analysis; Albedo optimization; absorptance spectra of nonwoven cotton fiber layer and pure CA film; reflectance spectra of pure CA film and solvent-quenched CA film; reflectance spectra of the laminated cotton scaffold and cooling geotextile; FDTD model and results; diffuse reflection spectrum of cooling geotextile; Kubelka−Munk (K−M) spectra of cooling geotextile, wet soil, and dried soil; solar heating powers of soils with different water contents; bar plot of albedo for cooling geotextile and different natural substances; FTIR absorbance spectra of soil, nonwoven layer, and cooling geotextile; solar heating/radiative cooling power of the soil and cooling geotextile; surface temperature simulation; real-time soil temperature measurement data; solar intensity data for selected Arctic regions; thermal conductivity of the cooling geotextile; water absorption data and evaporative power estimation; photos and schematics of application of cooling geotextile on the bare ground; simulated static structural vertical deformation of the cooling geotextile under different wind speed; the maximum thickness of the air gaps with different wind speeds at the side and the center of the cooling geotextile in the air dynamic simulation; LPJ-STM simulation under RCP 2.6 scenario; simulated average soil temperature profile of the Arctic bare ground; predicted permafrost depth without and with cooling geotextile; pan-Arctic infrastructure hazard map without or with cooling geotextile under RCP 2.6 scenario; simulation of pan-Arctic bare ground temperature and permafrost content considering different air layer thicknesses between the cooling geotextile and the bare ground; mesh plot of the volumetric heat capacity of soil; schematic and data of carbon cycle considering permafrost thawing in the Arctic; $^{1}$H NMR spectra of CA; cost and carbon footprint analysis table; mechanical strength and permittivity requirements for the geotextile; comparative analysis; properties of selected biodegradable geotextiles; and parameters and values in soil volumetric heat capacity and heat transfer (PDF)

## AUTHOR INFORMATION


### Corresponding Author

**Tian Li** − *School of Mechanical Engineering, Purdue University, West Lafayette, Indiana 47907, United States;* orcid.org/0000-0002-1087-0662; Email: tianli@purdue.edu

### Authors

**Wenhui Xu** − *School of Mechanical Engineering, Purdue University, West Lafayette, Indiana 47907, United States;* orcid.org/0000-0002-6853-0548

**Xiaojie Liu** − *School of Mechanical Engineering, Purdue University, West Lafayette, Indiana 47907, United States*

**Wei Yan** − *State Key Laboratory of Advanced Fiber Materials, College of Materials Science and Engineering, Donghua University, Shanghai 201620, P. R. China;* orcid.org/0000-0003-4646-7039

**Yanpei Tian** − *School of Mechanical Engineering, Purdue University, West Lafayette, Indiana 47907, United States*

**Yiming Xu** − *Department of Earth, Atmospheric, and Planetary Sciences, Purdue University, West Lafayette, Indiana 47907, United States*

**Wenkai Zhu** − *School of Mechanical Engineering, Purdue University, West Lafayette, Indiana 47907, United States*

**Noor M. Mohammad** − *School of Mechanical Engineering, Purdue University, West Lafayette, Indiana 47907, United States*

**Zhenyuan Niu** − *School of Mechanical Engineering, Purdue University, West Lafayette, Indiana 47907, United States*

**Ya Liu** − *State Key Laboratory of Advanced Fiber Materials, College of Materials Science and Engineering, Donghua University, Shanghai 201620, P. R. China*

**Pengfei Deng** − *School of Mechanical Engineering, Purdue University, West Lafayette, Indiana 47907, United States*

**Qilong Cheng** − *School of Mechanical Engineering, Purdue University, West Lafayette, Indiana 47907, United States;* orcid.org/0000-0002-1281-2204

**Fengyin Du** − *School of Mechanical Engineering, Purdue University, West Lafayette, Indiana 47907, United States*




https://doi.org/10.1021/acsnano.5c06567
ACS Nano 2025, 19, 40774−40788

**Jinlong He** − *Department of Mechanical Engineering, University of Wisconsin-Madison, Madison, Wisconsin 53706, United States;* orcid.org/0009-0006-5171-3694
**Hengxue Xiang** − *State Key Laboratory of Advanced Fiber Materials, College of Materials Science and Engineering, Donghua University, Shanghai 201620, P. R. China;* orcid.org/0000-0002-7576-9434
**Ying Li** − *Department of Mechanical Engineering, University of Wisconsin-Madison, Madison, Wisconsin 53706, United States;* orcid.org/0000-0002-1487-3350
**Jeffrey P. Youngblood** − *School of Materials Engineering, Purdue University, West Lafayette, Indiana 47907, United States;* orcid.org/0000-0002-8720-8642
**Nathan T. Kurtz** − *Cryospheric Sciences Laboratory, NASA Goddard Space Flight Center, Greenbelt, Maryland 20771, United States*
**Meifang Zhu** − *State Key Laboratory of Advanced Fiber Materials, College of Materials Science and Engineering, Donghua University, Shanghai 201620, P. R. China*
**Qianlai Zhuang** − *Department of Earth, Atmospheric, and Planetary Sciences, Purdue University, West Lafayette, Indiana 47907, United States*

Complete contact information is available at: https://pubs.acs.org/10.1021/acsnano.5c06567

### Author Contributions

[▽]W.X., X.L., W.Y. and Y.T. contributed equally to this work. T.L. conceived and supervised the project and provided guidance on experiments and writing. W.X. designed and fabricated the cooling geotextile with input from T.L., X.L., and W.Y. W.X. designed and conducted optical, mechanical, biodegradation, and field tests, and performed heat transfer and optical simulations. W.X., X.L., and Y.T. cowrote the manuscript with input from all coauthors. X.L. and Y.T. contributed substantially to manuscript writing and figure reorganization. W.Y. and M.Z. designed and realized large-scale roll-to-roll manufacturing of the cooling geotextile. Y.X. and Q.Z. performed global modeling; Y.X. analyzed climate data, and Q.Z. supervised the modeling and provided insights. W.Z. provided and helped with radiative cooling calculation. N.M.M. conducted life cycle analysis and assisted with field tests. Z.N. performed air gap simulations and assisted with NMR. Y.L. and H.X. contributed to roll-to-roll manufacturing. P.D. measured thermal conductivity. Q.C. built the photovoltaic model and provided revision suggestions for the introduction. F.D. performed mercury intrusion porosimetry. J.H. and Y. Li performed MD and SMD simulations. J.Y. contributed to materials processing. N.T.K. provided cryospheric science insights and satellite photos.

### Notes

The authors declare the following competing financial interest(s): The cooling geotextile is being commercialized by Watex LLC, a company founded by the corresponding author.

## ACKNOWLEDGMENTS

We would like to thank Robbin Garber-Slaght for her valuable Arctic field expertise and for providing field photographs. We are also grateful to Dr. Jody Tishimack for supplying compost soil and sharing her insights into soil biodegradation.

## REFERENCES

(1) Zhang, T.; Barry, R. G.; Knowles, K.; Heginbottom, J. A.; Brown, J. Statistics and Characteristics of Permafrost and Ground-Ice Distribution in the Northern Hemisphere. *Polar Geogr.* **2008**, *31* (1−2), 47−68.
(2) Schuur, E. A. G.; McGuire, A. D.; Schädel, C.; Grosse, G.; Harden, J. W.; Hayes, D. J.; Hugelius, G.; Koven, C. D.; Kuhry, P.; Lawrence, D. M.; Natali, S. M.; Olefeldt, D.; Romanovsky, V. E.; Schaefer, K.; Turetsky, M. R.; Treat, C. C.; Vonk, J. E. Climate Change and the Permafrost Carbon Feedback. *Nature* **2015**, *520* (7546), 171−179.
(3) Zimov, S. A.; Schuur, E. A. G.; Chapin, F. S., III Permafrost and the Global Carbon Budget. *Science* **2006**, *312*, 1612−1614.
(4) Huge Permafrost Thaw Can Be Limited by Ambitious Climate Targets. https://www.leeds.ac.uk/news-environment/news/article/4032/huge-permafrost-thaw-can-be-limited-by-ambitious-climate-targets. (accessed Jan 01, 2025).
(5) Armstrong McKay, D. I.; Staal, A.; Abrams, J. F.; Winkelmann, R.; Sakschewski, B.; Loriani, S.; Fetzer, I.; Cornell, S. E.; Rockström, J.; Lenton, T. M. Exceeding 1.5°C Global Warming Could Trigger Multiple Climate Tipping Points. *Science* **2022**, *377* (6611), No. eabn7950.
(6) Smith, S. L.; O'Neill, H. B.; Isaksen, K.; Noetzli, J.; Romanovsky, V. E. The Changing Thermal State of Permafrost. *Nat. Rev. Earth Environ.* **2022**, *3* (1), 10−23.
(7) Turetsky, M. R.; Jones, M. C.; Walter Anthony, K.; Olefeldt, D.; Schuur, E. A. G.; Koven, C.; Mcguire, A. D.; Grosse, G.; et al. Permafrost Collapse Is Accelerating Carbon Release. *Nature* **2019**, *569*, 32−34.
(8) Martens, J.; Wild, B.; Muschitiello, F.; O'Regan, M.; Jakobsson, M.; Semiletov, I.; Dudarev, O. V.; Gustafsson, Ö. Remobilization of Dormant Carbon from Siberian-Arctic Permafrost during Three Past Warming Events. *Sci. Adv.* **2020**, *6* (42), No. eabb6546.
(9) Miner, K. R.; D'Andrilli, J.; Mackelprang, R.; Edwards, A.; Malaska, M. J.; Waldrop, M. P.; Miller, C. E. Emergent Biogeochemical Risks from Arctic Permafrost Degradation. *Nat. Clim. Change* **2021**, *11* (10), 809−819.
(10) Hutchins, D. A.; Jansson, J. K.; Remais, J. V.; Rich, V. I.; Singh, B. K.; Trivedi, P. Climate Change Microbiology — Problems and Perspectives. *Nat. Rev. Microbiol.* **2019**, *17* (6), 391−396.
(11) Ewing, S. A.; Paces, J. B.; O'Donnell, J. A.; Jorgenson, M. T.; Kanevskiy, M. Z.; Aiken, G. R.; Shur, Y.; Harden, J. W.; Striegl, R. Uranium Isotopes and Dissolved Organic Carbon in Loess Permafrost: Modeling the Age of Ancient Ice. *Geochim. Cosmochim. Acta* **2015**, *152*, 143−165.
(12) Aslam, S. N.; Huber, C.; Asimakopoulos, A. G.; Steinnes, E.; Mikkelsen, Ø. Trace Elements and Polychlorinated Biphenyls (PCBs) in Terrestrial Compartments of Svalbard, Norwegian Arctic. *Sci. Total Environ.* **2019**, *685*, 1127−1138.
(13) Hjort, J.; Streletskiy, D.; Doré, G.; Wu, Q.; Bjella, K.; Luoto, M. Impacts of Permafrost Degradation on Infrastructure. *Nat. Rev. Earth Environ.* **2022**, *3* (1), 24−38.
(14) Schuur, E. A. G.; Abbott, B. Climate Change: High Risk of Permafrost Thaw. *Nature* **2011**, *480* (7375), 32−33.
(15) Irrgang, A. M.; Bendixen, M.; Farquharson, L. M.; Baranskaya, A. V.; Erikson, L. H.; Gibbs, A. E.; Ogorodov, S. A.; Overduin, P. P.; Lantuit, H.; Grigoriev, M. N.; Jones, B. M. Drivers, Dynamics and Impacts of Changing Arctic Coasts. *Nat. Rev. Earth Environ.* **2022**, *3* (1), 39−54.
(16) Vonk, J. E.; Gustafsson, O. Permafrost-Carbon Complexities. *Nat. Geosci.* **2013**, *6* (9), 675−676.
(17) Field, C. B.; Raupach, M. R. *The Global Carbon Cycle: Integrating Humans, Climate, and the Natural World*; Island Press, 2004; Vol. *62*.
(18) Schuur, E. A. G.; Bockheim, J.; Canadell, J. G.; Euskirchen, E.; Field, C. B.; Goryachkin, S. V.; Hagemann, S.; Kuhry, P.; Lafleur, P. M.; Lee, H.; Mazhitova, G.; Nelson, F. E.; Rinke, A.; Romanovsky, V. E.; Shiklomanov, N.; Tarnocai, C.; Venevsky, S.; Vogel, J. G.; Zimov, S. A. Vulnerability of Permafrost Carbon to Climate Change:

Implications for the Global Carbon Cycle. *Bioscience* **2008**, *58* (8), 701−714.
(19) Sehmel, T.; Strunk, R. Potential Mitigation Strategies for Buildings and Infrastructure on Thawing Permafrost. http://cchrc.org/media/PotentialMitigationStrategies-OneHealthConference-2021.pdf. (accessed Jan 05, 2025).
(20) Chen, Y.; Liu, A.; Moore, J. C. Mitigation of Arctic Permafrost Carbon Loss through Stratospheric Aerosol Geoengineering. *Nat. Commun.* **2020**, *11* (1), No. 2430.
(21) Feklistov, V. N.; Rusakov, N. L. Application of Foam Insulation for Remediation of Degraded Permafrost. *Cold Reg. Sci. Technol.* **1996**, *24* (2), 205−212.
(22) Regehr, J. D.; Milligan, C. A.; Montufar, J.; Alfaro, M. Review of Effectiveness and Costs of Strategies to Improve Roadbed Stability in Permafrost Regions. *J. Cold Reg. Eng.* **2013**, *27* (3), 109−131.
(23) Hoopes, O.; Croft, P.; Wuttig, F.; Schulz, C.; Mathieson, W. In *Embankment Fill Slope Movement on Thaw Sensitive Permafrost: Combining Creep Testing and Thermal Simulations to Develop Mitigation Options at Lost Creek along the Trans-Alaska Pipeline System; Lost Creek-Part 2*, PERMAFROST 2021: Merging Permafrost Science and Cold Regions Engineering; ASCE, 2021; pp 360−373.
(24) Wang, Y.; Jin, H.; Li, G. Investigation of the Freeze-Thaw States of Foundation Soils in Permafrost Areas along the China-Russia Crude Oil Pipeline (CRCOP) Route Using Ground-Penetrating Radar (GPR). *Cold Reg. Sci. Technol.* **2016**, *126*, 10−21.
(25) Zhi, W.; Yu, S.; Wei, M.; Jilin, Q.; Wu, J. Analysis on Effect of Permafrost Protection by Two-Phase Closed Thermosyphon and Insulation Jointly in Permafrost Regions. *Cold Reg. Sci. Technol.* **2005**, *43* (3), 150−163.
(26) Wagner, A. M. *Review of Thermosyphon Applications*; Cold Regions Research and Engineering Laboratory: US, 2014.
(27) Textile Glacier Protection. https://texpertisenetwork.messefrankfurt.com/frankfurt/en/news-stories/stories/textile-glacier-protection.html. (accessed July 05, 2025).
(28) Glacier protection with Geotextiles—A Sustainable Solution for the Future. https://www.naue.com/es/glacier-protection-with-geotextiles-a-sustainable-solution-for-the-future/. (accessed July 05, 2025).
(29) Isabel Amos-Landgraf. Geotextiles Could Slow Glacial Melt, but at What Cost?. State of the Planet. https://news.climate.columbia.edu/2021/04/14/geotextiles-slow-glacial-melt-cost/. (accessed February 01, 2023).
(30) Li, J.; Liang, Y.; Li, W.; Xu, N.; Zhu, B.; Wu, Z.; Wang, X.; Fan, S.; Wang, M.; Zhu, J. Protecting Ice from Melting under Sunlight via Radiative Cooling. *Sci. Adv.* **2022**, *8* (6), No. eabj9756.
(31) Betts, A. K.; Ball, J. H. Albedo over the Boreal Forest. *J. Geophys. Res.: Atmos.* **1997**, *102* (D24), 28901−28909.
(32) Brandt, R. E.; Warren, S. G.; Worby, A. P.; Grenfell, T. C. Surface Albedo of the Antarctic Sea Ice Zone. *J. Clim.* **2005**, *18* (17), 3606−3622.
(33) Charlson, R. J.; Lovelock, J. E.; Andreaei, M. O.; Warren, S. G. Oceanic Phytoplankton, Atmospheric Sulphur, Cloud Albedo and Climate. *Nature* **1987**, *326*, 655−661.
(34) Hall, D. *Remote Sensing of Ice and Snow*; Springer Science & Business Media, 2012.
(35) Aartsma, P.; Asplund, J.; Odland, A.; Reinhardt, S.; Renssen, H. Surface Albedo of Alpine Lichen Heaths and Shrub Vegetation. *Arctic, Antarct. Alp. Res.* **2020**, *52* (1), 312−322.
(36) Prambauer, M.; Wendeler, C.; Weitzenböck, J.; Burgstaller, C. Biodegradable Geotextiles−An Overview of Existing and Potential Materials. *Geotext. Geomembr.* **2019**, *47* (1), 48−59.
(37) Daria, M.; Krzysztof, L.; Jakub, M. Characteristics of Biodegradable Textiles Used in Environmental Engineering: A Comprehensive Review. *J. Cleaner Prod.* **2020**, *268*, No. 122129.
(38) Wu, H.; Yao, C.; Li, C.; Miao, M.; Zhong, Y.; Lu, Y.; Liu, T. Review of Application and Innovation of Geotextiles in Geotechnical Engineering. *Materials* **2020**, *13* (7), No. 1774.
(39) Glooschenko, W. A.; Tarnocai, C.; Zoltai, S.; Glooschenko, V. *Wetlands of Canada and Greenland BT - Wetlands of the World: Inventory, Ecology and Management Vol. I: Africa, Australia, Canada and Greenland, Mediterranean, Mexico, Papua New Guinea, South Asia, Tropical South America, United States*; Whigham, D. F.; Dykyjová, D.; Hejný, S., Eds.; Springer: Dordrecht, 1993; pp 415−514.
(40) Osterkamp, T. E.; Jorgenson, M. T.; Schuur, E. A. G.; Shur, Y. L.; Kanevskiy, M. Z.; Vogel, J. G.; Tumskoy, V. E. Physical and Ecological Changes Associated with Warming Permafrost and Thermokarst in Interior Alaska. *Permafrost Periglacial Processes* **2009**, *20* (3), 235−256.
(41) Murton, J. B. Global Warming and Thermokarst. *Permafr. Soils* **2009**, *16*, 185−203.
(42) Günther, F.; Overduin, P. P.; Sandakov, A. V.; Grosse, G.; Grigoriev, M. N. Short-and Long-Term Thermo-Erosion of Ice-Rich Permafrost Coasts in the Laptev Sea Region. *Biogeosciences* **2013**, *10* (6), 4297−4318.
(43) Swanson, D. K. Permafrost Thaw-related Slope Failures in Alaska's Arctic National Parks, c. 1980−2019. *Permafrost Periglacial Processes* **2021**, *32* (3), 392−406.
(44) Patton, A. I.; Rathburn, S. L.; Capps, D. M.; McGrath, D.; Brown, R. A. Ongoing Landslide Deformation in Thawing Permafrost. *Geophys. Res. Lett.* **2021**, *48* (16), No. e2021GL092959.
(45) Arctic System Reanalysis Version 2. Research Data Archive at the National Center for Atmospheric Research, Computational and Information Systems Laboratory: Boulder, CO. (accessed Aug 21, 2023).
(46) Hsieh, Y.-L.Chemical Structure and Properties of Cotton. In *Cotton: Science and Technology*; Woodhead Publishing, 2007; pp 3−34.
(47) Avila, A. G.; Hinestroza, J. P. Tough Cotton. *Nat. Nanotechnol.* **2008**, *3* (8), 458−459.
(48) Šturcová, A.; Davies, G. R.; Eichhorn, S. J. Elastic Modulus and Stress-Transfer Properties of Tunicate Cellulose Whiskers. *Biomacromolecules* **2005**, *6* (2), 1055−1061.
(49) Dufresne, A. *Nanocellulose: From Nature to High Performance Tailored Materials*; Walter de Gruyter GmbH & Co KG, 2017.
(50) Xiang, P.; Kuznetsov, A. V.; Seyam, A. M. A Porous Medium Model of the Hydroentanglement Process. *J. Porous Media* **2008**, *11* (1), 35−49.
(51) Brennan, J. P.; Sporing, L. C. Process and Apparatus for Preparing a Molded, Textured, Spunlaced, Nonwoven Web. U.S. Patent US7,530,150B2, 2009.
(52) Burg, S. L.; Washington, A.; Coles, D. M.; Bianco, A.; McLoughlin, D.; Mykhaylyk, O. O.; Villanova, J.; Dennison, A. J. C.; Hill, C. J.; Vukusic, P.; Doak, S.; Martin, S. J.; Hutchings, M.; Parnell, S. R.; Vasilev, C.; Clarke, N.; Ryan, A. J.; Furnass, W.; Croucher, M.; Dalgliesh, R. M.; Prevost, S.; Dattani, R.; Parker, A.; Jones, R. A. L.; Fairclough, J. P. A.; Parnell, A. J. Liquid−Liquid Phase Separation Morphologies in Ultra-White Beetle Scales and a Synthetic Equivalent. *Commun. Chem.* **2019**, *2* (1), No. 100.
(53) Irannezhad, M.; Marttila, H.; Ahmadi, B. *Impacts of Climate Extremes over Arctic and Antarctic*; Elsevier Inc., 2022; Vol. *2*.
(54) Hall, A. The Role of Surface Albedo Feedback in Climate. *J. Clim.* **2004**, *17* (7), 1550−1568.
(55) Bormann, K. J.; Brown, R. D.; Derksen, C.; Painter, T. H. Estimating Snow-Cover Trends from Space. *Nat. Clim. Change* **2018**, *8* (11), 924−928.
(56) Li, T.; Zhai, Y.; He, S.; Gan, W.; Wei, Z.; Heidarinejad, M.; Dalgo, D.; Mi, R.; Zhao, X.; Song, J.; Dai, J.; Chen, C.; Aili, A.; Vellore, A.; Martini, A.; Yang, R.; Srebric, J.; Yin, X.; Hu, L. A Radiative Cooling Structural Material. *Science* **2019**, *364* (6442), 760−763.
(57) Orelma, H.; Hokkanen, A.; Leppänen, I.; Kammiovirta, K.; Kapulainen, M.; Harlin, A. Optical Cellulose Fiber Made from Regenerated Cellulose and Cellulose Acetate for Water Sensor Applications. *Cellulose* **2020**, *27* (3), 1543−1553.
(58) Kaijanen, L.; Paakkunainen, M.; Pietarinen, S.; Jernström, E.; Reinikainen, S.-P. Ultraviolet Detection of Monosaccharides: Multiple Wavelength Strategy to Evaluate Results after Capillary Zone


https://doi.org/10.1021/acsnano.5c06567
*ACS Nano* 2025, 19, 40774−40788

Electrophoretic Separation. *Int. J. Electrochem. Sci.* **2015**, *10* (4), 2950−2961.
(59) Rowen, J. W.; Hunt, C. M.; Plyler, E. K. Absorption Spectra in the Detection of Chemical Changes in Cellulose and Cellulose Derivatives. *Text. Res. J.* **1947**, *17* (9), 504−511.
(60) Mandal, J.; Fu, Y.; Overvig, A. C.; Jia, M.; Sun, K.; Shi, N. N.; Zhou, H.; Xiao, X.; Yu, N.; Yang, Y. Hierarchically Porous Polymer Coatings for Highly Efficient Passive Daytime Radiative Cooling. *Science* **2018**, *362* (6412), 315−319.
(61) Rana, A.; Dey, S.; Sarkar, S. Optical Properties of Brown Carbon in Aerosols and Surface Snow at Ny-Ålesund during the Polar Summer. In *Understanding Present and Past Arctic Environments*; Elsevier, 2021.
(62) Li, D.; Liu, X.; Li, W.; Lin, Z.; Zhu, B.; Li, Z.; Li, J.; Li, B.; Fan, S.; Xie, J.; Zhu, J. Scalable and Hierarchically Designed Polymer Film as a Selective Thermal Emitter for High-Performance All-Day Radiative Cooling. *Nat. Nanotechnol.* **2021**, *16* (2), 153−158.
(63) Hu, T.-f.; Yue, Z. Potential Applications of Solar Refrigeration Systems for Permafrost Cooling in Embankment Engineering. *Case Stud. Therm. Eng.* **2021**, *26*, No. 101086.
(64) Chen, L.; Yu, W.; Lu, Y.; Wu, P.; Han, F. Characteristics of Heat Fluxes of an Oil Pipeline Armed with Thermosyphons in Permafrost Regions. *Appl. Therm. Eng.* **2021**, *190*, No. 116694.
(65) Mu, Y.; Li, G.; Yu, Q.; Ma, W.; Wang, D.; Wang, F. Numerical Study of Long-Term Cooling Effects of Thermosyphons around Tower Footings in Permafrost Regions along the Qinghai-Tibet Power Transmission Line. *Cold Reg. Sci. Technol.* **2016**, *121*, 237−249.
(66) Wagner, A. M.; Yarmak Edward, J. In *The Performance of Artificial Frozen Barriers*; ISCORD 2013: Planning for Sustainable Cold Regions; ASCE, 2013; pp 116−127.
(67) Qin, Y.; Zhang, J. A Review on the Cooling Effect of Duct-Ventilated Embankments in China. *Cold Reg. Sci. Technol.* **2013**, *95*, 1−10.
(68) Sun, Z.; Liu, J.; Hu, T.; You, T.; Fang, J. A Solar Compression Refrigeration Apparatus to Cool Permafrost Embankment. *Appl. Therm. Eng.* **2023**, *223*, No. 120034.
(69) Ahankari, S.; Paliwal, P.; Subhedar, A.; Kargarzadeh, H. Recent Developments in Nanocellulose-Based Aerogels in Thermal Applications: A Review. *ACS Nano* **2021**, *15* (3), 3849−3874.
(70) Lei, L.; Shi, S.; Wang, D.; Meng, S.; Dai, J.-G.; Fu, S.; Hu, J. Recent Advances in Thermoregulatory Clothing: Materials, Mechanisms, and Perspectives. *ACS Nano* **2023**, *17* (3), 1803−1830.
(71) Raman, A. P.; Anoma, M. A.; Zhu, L.; Rephaeli, E.; Fan, S. Passive Radiative Cooling below Ambient Air Temperature under Direct Sunlight. *Nature* **2014**, *515* (7528), 540−544.
(72) Ross, T. F.National Solar Radiation Data Base Hourly Solar Data from Alaska. 2016, pp 1961−1990. No. Arctic Data Center.
(73) Jiang, Y.; Zhuang, Q.; Sitch, S.; O'Donnell, J. A.; Kicklighter, D.; Sokolov, A.; Melillo, J. Importance of Soil Thermal Regime in Terrestrial Ecosystem Carbon Dynamics in the Circumpolar North. *Glob. Planet. Change* **2016**, *142*, 28−40.
(74) Jiang, Y.; Zhuang, Q.; O'Donnell, J. A. Modeling Thermal Dynamics of Active Layer Soils and Near-Surface Permafrost Using a Fully Coupled Water and Heat Transport Model. *J. Geophys. Res.: Atmos.* **2012**, *117* (11), 1−15.
(75) Sitch, S.; Smith, B.; Prentice, I. C.; Arneth, A.; Bondeau, A.; Cramer, W.; Kaplan, J. O.; Levis, S.; Lucht, W.; Sykes, M. T.; et al. Evaluation of Ecosystem Dynamics, Plant Geography and Terrestrial Carbon Cycling in the LPJ Dynamic Global Vegetation Model. *Global Change Biol.* **2003**, *9* (2), 161−185.
(76) Gerten, D.; Schaphoff, S.; Haberlandt, U.; Lucht, W.; Sitch, S. Terrestrial Vegetation and Water Balance - Hydrological Evaluation of a Dynamic Global Vegetation Model. *J. Hydrol.* **2004**, *286* (1−4), 249−270.
(77) Pachauri, R. K.; Meyer, L. A. *Climate Change 2014: Synthesis Report. Contribution of Working Groups I, II and III to the Fifth Assessment Report of the Intergovernmental Panel on Climate Change*, IPCC, 2014.
(78) Hersbach, H.; Bell, B.; Berrisford, P.; Biavati, G.; Horányi, A.; Muñoz Sabater, J.; Nicolas, J.; Peubey, C.; Radu, R.; Rozum, I.; Schepers, D.; Simmons, A.; Soci, C.; Dee, D.; Thépaut, J.-N. ERA5 monthly averaged data on single levels from 1979 to present. Copernicus Climate Change Service (C3S) Climate Data Store (CDS). 2019 DOI: 10.24381/cds.f17050d7.
(79) Mueller, C. W.; Rethemeyer, J.; Kao-Kniffin, J.; Löppmann, S.; Hinkel, K. M.; Bockheim, J. G. Large Amounts of Labile Organic Carbon in Permafrost Soils of Northern Alaska. *Global Change Biol.* **2015**, *21* (7), 2804−2817.
(80) Saaty, R. W. The Analytic Hierarchy Process-What It Is and How It Is Used. *Math. Model.* **1987**, *9* (3−5), 161−176.
(81) Hjort, J.; Karjalainen, O.; Aalto, J.; Westermann, S.; Romanovsky, V. E.; Nelson, F. E.; Etzelmüller, B.; Luoto, M. Degrading Permafrost Puts Arctic Infrastructure at Risk by Mid-Century. *Nat. Commun.* **2018**, *9* (1), No. 5147.
(82) Shahabi, H.; Hashim, M. Landslide Susceptibility Mapping Using GIS-Based Statistical Models and Remote Sensing Data in Tropical Environment. *Sci. Rep.* **2015**, *5* (1), No. 9899.
(83) Farr, T. G.; Rosen, P. A.; Caro, E.; Crippen, R.; Duren, R.; Hensley, S.; Kobrick, M.; Paller, M.; Rodriguez, E.; Roth, L.et al. The Shuttle Radar Topography Mission *Rev. Geophys.* 2007; Vol. *45* 2.
(84) Brown, J.; Ferrians, O.; Heginbottom, J. A.; Circum-Arctic, E. M. *Map of Permafrost and Ground-Ice Conditions, Version 2. Boulder, Colorado USA*; No. National Snow and Ice Data Center, 2002.
(85) Hengl, T.; de Jesus, J. M.; MacMillan, R. A.; Batjes, N. H.; Heuvelink, G. B. M.; Ribeiro, E.; Samuel-Rosa, A.; Kempen, B.; Leenaars, J. G. B.; Walsh, M. G.; Gonzalez, M. R. SoilGrids1km—Global Soil Information Based on Automated Mapping. *PLoS One* **2014**, *9* (8), No. e105992.
(86) Hong, E.; Perkins, R.; Trainor, S. Thaw Settlement Hazard of Permafrost Related to Climate Warming in Alaska. *Arctic* **2014**, *67*, 93−103.
(87) Turetsky, M. R.; Abbott, B. W.; Jones, M. C.; Anthony, K. W.; Olefeldt, D.; Schuur, E. A. G.; Grosse, G.; Kuhry, P.; Hugelius, G.; Koven, C.; et al. Carbon Release through Abrupt Permafrost Thaw. *Nat. Geosci.* **2020**, *13* (2), 138−143.
(88) Miner, K. R.; Turetsky, M. R.; Malina, E.; Bartsch, A.; Tamminen, J.; McGuire, A. D.; Fix, A.; Sweeney, C.; Elder, C. D.; Miller, C. E. Permafrost Carbon Emissions in a Changing Arctic. *Nat. Rev. Earth Environ.* **2022**, *3* (1), 55−67.
(89) Nikitin, D. A.; Lysak, L. V.; Mergelov, N. S.; Dolgikh, A. V.; Zazovskaya, E. P.; Goryachkin, S. V. Microbial Biomass, Carbon Stocks, and CO 2 Emission in Soils of Franz Josef Land: High-Arctic Tundra or Polar Deserts? *Eurasian Soil Sci.* **2020**, *53*, 467−484.
(90) Brummell, M. E.; Farrell, R. E.; Hardy, S. P.; Siciliano, S. D. Greenhouse Gas Production and Consumption in High Arctic Deserts. *Soil Biol. Biochem.* **2014**, *68*, 158−165.
(91) Peltola, O.; Vesala, T.; Gao, Y.; Räty, O.; Alekseychik, P.; Aurela, M.; Chojnicki, B.; Desai, A. R.; Dolman, A. J.; Euskirchen, E. S.; et al. Monthly Gridded Data Product of Northern Wetland Methane Emissions Based on Upscaling Eddy Covariance Observations. *Earth Syst. Sci. Data* **2019**, *11* (3), 1263−1289.
(92) Bruhwiler, L.; Parmentier, F.-J. W.; Crill, P.; Leonard, M.; Palmer, P. I. The Arctic Carbon Cycle and Its Response to Changing Climate. *Curr. Clim. Change Reports* **2021**, *7*, 14−34.
(93) Schuur, T.; McGuire, A. D.; Romanovsky, V.; Schädel, C.; Mack, M.*SOCCR2 Chapter 11: Arctic and Boreal Carbon. Second State of the Carbon Cycle Report*; National Academies Press, 2018; 428-468.
(94) Marconnet, A. M.; Yamamoto, N.; Panzer, M. A.; Wardle, B. L.; Goodson, K. E. Thermal Conduction in Aligned Carbon Nanotube-Polymer Nanocomposites with High Packing Density. *ACS Nano* **2011**, *5* (6), 4818−4825.


https://doi.org/10.1021/acsnano.5c06567
*ACS Nano* 2025, 19, 40774−40788